Modelling the effect of the tidal cycle on the high phytoplankton biomass area of Cape Trafalgar (SW Iberian Peninsula)

Iria Sala, Sergio M Vallina, Marina Lévy, Marina Bolado-Penagos, Carlos M García, Fidel Echevarría, José C Sánchez-Garrido

Modelling the effect of the tidal cycle on the high phytoplankton biomass area of Cape Trafalgar (SW Iberian Peninsula)

Iria Sala[a,b,*], Sergio M. Vallina[c], Marina Lévy[d], Marina Bolado-Penagos[e], Carlos M. García[a], Fidel Echevarría[a], José C. Sánchez-Garrido[f]

[a]*Departamento de Biología, Facultad de Ciencias del Mar y Ambientales, Instituto Universitario de Investigación Marina (INMAR), Campus de Excelencia Internacional del Mar (CEI-MAR), Universidad de Cádiz, Puerto Real, 11510 Cádiz, Spain*

[b]*Department of Mathematics and Statistics, University of Strathclyde, G1 1XH Glasgow, United Kingdom*

[c]*Instituto Español de Oceanografía (IEO – CSIC), 33212 Gijón, Asturias, Spain*

[d]*Sorbonne Université, Laboratoire d'Océanographie et du Climat, Institut Pierre Simon Laplace (LOCEAN, SU/CNRS/IRD/MNHN), 75252 Paris Cedex 05, France*

[e]*Departamento de Física Aplicada, Facultad de Ciencias del Mar y Ambientales, Instituto Universitario de Investigación Marina (INMAR), Campus de Excelencia Internacional del Mar (CEI-MAR), Universidad de Cádiz, 11510 Puerto Real, Cádiz, Spain*

[f]*Grupo de Oceanografía Física, Universidad de Málaga, 29016 Málaga, Spain*

Abstract

Physical-biological interactions in the ocean are known to be crucial for understanding ecosystem processes. This is particularly relevant in the highly dynamic coastal regions, where the biogeochemical processes associated with higher-frequency perturbations such as tidal waves play a key role in primary production. In this study, we examine the influence of the tide-topography interaction on the high productivity area of Cape Trafalgar (NW limit of the Strait of Gibraltar, Iberian Peninsula) using a high-resolution ocean circulation model coupled to an ecosystem model. The obtained results highlight the relevance of the tidal cycle explaining the high phytoplankton biomass that characterises this region through an active and periodic forcing, resulting in a pulsating upwelling system. Our model shows that the interaction of the westward zonal component of the tidal current (uvel) with the submarine ridge (i.e., Barbate High) that characterises this region, which is perpendicular to the coast, results in the pumping of deep, cold, salty, and nutrient-rich waters to the well-illuminated subsurface waters, fuelling phytoplankton growth. At the same time, the interaction of the westward tidal current with the ridge leads to the development of a cyclonic eddy, which enables the redistribution of the upwelled waters over and to the east of Barbate High. The fortnightly tidal period has been identified as the most influential because (an effective) tidal-pumping process only takes place when the westward uvel is ~ 0.42 m s^{-1}, a condition attained between ~ 3 days before and after the moment of maximum tidal flow during spring tides. Simultaneously, the energy and the associated horizontal and vertical mixing of the cyclonic gyre also vary

*Corresponding author

Email addresses: iria.sala@gmail.com (Iria Sala)

with the tidal cycle, being stronger during spring tides. Both tidally driven processes, i.e., the cyclical upslope advection of deep nutrient-rich water and the influence of the cyclonic gyre, are the main mechanisms that lead to the development of a persistent phytoplankton-rich tongue over Barbate High. Consequently, Cape Trafalgar acts as a source of nutrient- and phytoplankton-rich waters to the surrounding waters.

Key words: tidal mixing, physical-biological coupled model, phytoplankton, Cape Trafalgar, Strait of Gibraltar

1. Introduction

Covering 6% of the world's surface, coastal waters are a vital part of the environment and provide between 22 and 43% of global ecosystem services (Costanza et al., 2014). The highly dynamic coastal regions and the associated biogeochemical processes play a key role in phytoplankton growth, being primary production between 3 to 5 times higher than in oceanic regions (Simpson and Sharples, 2012). In many coastal regions, tides are an important physical forcing factor with a major impact on primary production (Pingree and Griffiths, 1978; Daly and Smith, 1993; Otto et al., 1990). The tidal cycle is responsible for a series of periodic fluctuations at different time scales. The release on internal tidal waves causes a horizontal displacement of water masses and subsequent maxima in tidal current speed, at the same time that the associated current shear results in internal turbulent mixing (e.g., Holloway et al., 2001; Rippeth and Inall, 2002; Dale et al., 2003). Thus, locally, tide-topography interaction can have a significant impact on biological production by fertilisation of illuminated surface waters and the resuspension of phytoplankton cells and other particles, concomitant to the consequent vertical mixing (Pingree et al., 1981; New and Pingree, 1990; Hu et al., 2008; Sharples et al., 2007; Palmer et al., 2013).

This process is especially relevant in the Strait of Gibraltar (south of the Iberian Peninsula), a shallow and narrow channel that separates the Atlantic Ocean and the Mediterranean Sea (Figure 1). The Strait is characterised by (i) the semi-diurnal tidal cycle with a periodicity of 12 hours and 25 minutes, which results in a horizontal displacement of water that generates an increase in the current speed and the associated vertical mixing every 6 hours and 12 minutes; and (ii) the spring-neap tidal cycle with a periodicity of $\sim$ 15 days, related to the apogee-perigee cycle (29.50-day periodicity) (García-Lafuente et al., 1990). The interaction of the tidal current with the Strait's sharp topography generates undulatory processes (e.g., internal waves) that modify the nutrient budget by recirculation from deeper to shallower layers (e.g., Macías et al., 2007b; Ramírez-Romero et al., 2012; Sánchez-Garrido et al., 2015). However, due to the hydrodynamics of this region being characterised by the superficial inflow of Atlantic water towards the Mediterranean Sea, and by the short-residence time of the mixed waters within the channel (Macías et al., 2007a; Bruno et al., 2013), the biological impact of this tide-topography interaction results in a 40% increase of productivity, not in the Strait itself, but in the adjacent Alborán Sea (western-most basin of the Mediterranean Sea) (Sánchez-Garrido et al., 2015). Thus, although the Strait is characterised by low productivity due to the surface circulation pattern, this is not the case in the coastal Cape Trafalgar region located on its north-western limit (Figure 1b).

Cape Trafalgar has been highlighted in several studies as a hotspot of high chlorophyll concentration (e.g., Prieto et al., 1999; Echevarría et al., 2002; García et al., 2002; Navarro and Ruiz, 2006), with the along-shore tide-topography interaction being suggested as the main responsible process (Vargas-Yáñez et al., 2002; Sala et al., 2018). A distinctive feature of Cape Trafalgar is a submarine ridge, known as Barbate High (Figure 1b), that extends offshore perpendicular to the coast. Vargas-Yáñez et al. (2002), using a 2D-model, studied the capacity of the tide-topography interaction to reproduce a situation similar to the pool off Trafalgar. Although their model was very simple, it captured the vertical excursions of heat and nutrients produced by the tide-topography interaction, cooling, and fertilising areas around the topographic accident. Later, Sala et al. (2018) examined the chlorophyll-*a* (chl-*a*) dynamics in this region using 10 years of ocean colour images (MERIS sensor, 300 m full resolution). The authors found that Cape Trafalgar is characterised by a quasi-permanent high chl-*a* concentration, with an average value of 1.44 mg m^{-3} throughout the whole studied period. A Wavelet Power Spectrum analysis showed that the temporal variability of chl-*a* concentration in Trafalgar did not show any clear pattern of variability. However, when the covariation between the zonal component of the current speed (uvel) and the chl-*a* concentration was analysed with a Wavelet Coherence analysis, it was observed a strong covariation at the fortnightly tidal cycle. In comparison, the adjacent platform of the Gulf of Cádiz showed an average chl-*a* concentration of 0.79 mg m^{-3} with a seasonal variability (Sala et al., 2018). Furthermore, Bolado-Penagos et al. (2020) analysing the trajectory of several passive drifters released close to Cape Trafalgar, together with performing a series of hydrodynamic simulations, identified the formation of a cyclonic eddy on the eastern flank of Trafalgar. This cyclonic eddy increases the residence time of the upwelled nutrient-rich waters in the region, favouring the high chl-*a* concentration that characterises this biomass hotspot. Nevertheless, although the study by Sala et al. (2018) identified a strong covariation of chl-*a* concentration with the fortnightly tidal cycle, the study was unable to analyse in detail the influence of the tidal cycle on chl-*a* dynamics, due to an inadequate sampling resolution. Furthermore, satellite ocean colour imagery only shows the most superficial layer, making it impossible to analyse properly the influence of the tidal cycle on the phytoplankton community for the whole water column.

The correct description of physical processes and their coupling with phytoplankton growth is a complex issue in regions highly influenced by tidal forcing. On the one hand, as tidal currents become more intense, they will lead to a more active pumping of deep saltier water to shallow areas, with a nutrient enrichment of well-illuminated (i.e., euphotic) layers, and subsequent growth of primary producers with a given temporal delay of the order of days. On the other hand, the intensification of the tidal current leads to a more active horizontal mixing and dispersal, thus decreasing nutrient concentration or phytoplankton accumulation. These are two opposing mechanisms affecting the phytoplankton community that are driven by the same single process: tidal forcing. Thus, using a modelling approach is probably the best way to understand the dynamics of Cape Trafalgar, which is of great importance as a source of phytoplankton biomass in the surrounding waters. This study aims at performing accurate simulations of the study area to evaluate how the upwelling process mediated by the tide-topography interaction can affect the phytoplankton biomass in the area of Cape Trafalgar. Furthermore, our approach will allow us to study how

the seasonal variability that governs the adjacent Gulf of Cádiz may influence our region of interest. For these two purposes, we have implemented a high-resolution circulation model that computes the main tidal constituents, coupled to an ecosystem model.

2. Methodology

2.1. Circulation model

The physical model used in this study is the Massachusetts Institute of Technology general circulation model (MITgcm; Marshall et al., 1997a,b). The MITgcm solves the Boussinesq form of the Navier-Stokes equations for an incompressible fluid on a staggered C-grid, with level vertical coordinates, and partial cell representation of the bottom topography. A KPP (K-Profile Parametrization) scheme parametrizes the sub-grid-scale vertical diffusion by turbulence (Large et al., 1994). Temperature, salinity, and biochemical tracers are advected with a third-order direct-space-time scheme with a flux limiter to prevent negative values in the solutions (Hundsdorfer and Trompert, 1994). This numerical scheme is stable and sufficiently diffusive without explicit horizontal diffusion. The model configuration is similar to the one applied by Sánchez-Garrido et al. (2015), which uses a curvilinear grid that is squeezed into the Strait of Gibraltar and the Alborán Sea enhancing the resolution of both areas (Figure 1a). With a horizontal high resolution of ~ 0.50 km within the Strait, small-scale topographic features and processes are well captured, such as internal hydraulic jumps with the associated mixing and propagating internal waves. In the vertical dimension, there are 46 depth levels with increasing cell size from the surface to the bottom.

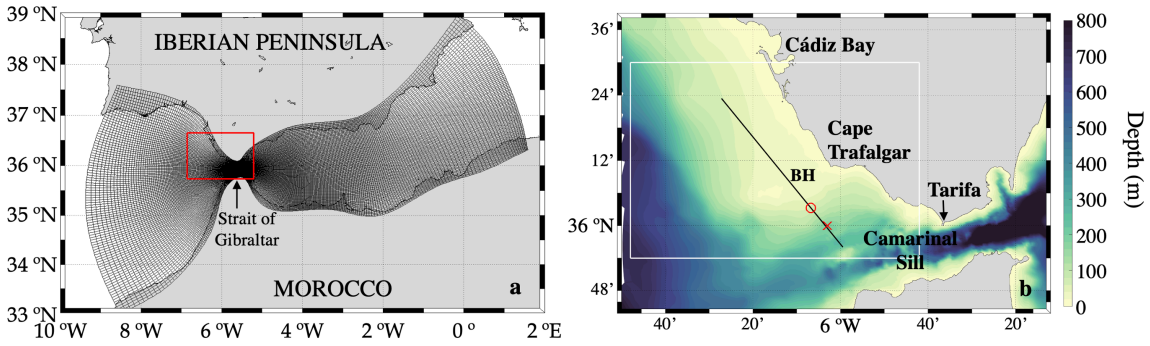

Figure 1: (a) Model domain and computational grid. The red rectangle encloses (b) a zoom of the region of interest. The spatial and temporal evolution of different variables (i.e., salinity, nitrate concentration and total phytoplankton biomass) are analysed at the Trafalgar region (enclosed by the white box), along the black line parallel to the coast, and at the point represented by the red circle. The red cross indicates the mooring position. BH: Barbate High. More details are in section 3.3.

Initial and boundary conditions were derived from the Iberia-Biscay-Ireland (IBI) Regional Seas reanalysis product from Copernicus Marine Environment Monitoring Service (CMEMS, http://marine.copernicus.eu/; Sotillo et al., 2015). Daily temperature, salinity and horizontal velocity fields were computed for the model lateral forcing. At the sea surface, the model is driven by wind stress, heat fluxes, freshwater flux from precipitation, and downward short-wave and long-wave radiation. All

these forcings were obtained from ERA-Interim and provided by the European Centre for Medium-range Weather Forecasts (ECMWF, https://www.ecmwf.int/; Dee et al., 2011). The atmospheric data has a time resolution of 6 hours and a spatial resolution of 0.125 degrees. The forcing fields for open boundary and atmospheric conditions correspond to the year 2010. We decided not to use a climatological year (i.e., the average of several selected years) because averaging smooths out daily fields and would result in an underestimation of submesoscale processes (Oguz et al., 2017). Latent and sensible heat fluxes are interactively calculated by the model using standard bulk formulas. Finally, tidal forcing is incorporated by prescribing time-dependent barotropic velocities across the open boundaries in association with the main eight tidal constituents in the region: the diurnal constituents, K1, O1, P1 and Q1, with periods of 23.93 h, 25.82 h, 24.07 h, and 26.87 h, respectively; and the semi-diurnal constituents M2, S2, N2, and K2, with periods of 12.42 h, 12.00 h, 12.66 h, and 11.97 h, respectively (García-Lafuente et al., 1990). This forcing yields a spring-neap tide cycle every 29.50 days, with the tidal range fluctuating from spring tide (maximum) to neap tide (minimum) and back to the spring tide. Moreover, the tidal range and the timing change daily, shifting by about 50 min per day (Ippen, 1966). Zero-flux and non-slip conditions are applied to all solid boundaries (i.e., bathymetry) together with a nonlinear bottom drag at the seafloor. The integration time step is 15 seconds. To obtain a stable (repeated seasonal cycle) solution of the circulation model, the simulation was run for 3 years. Two years of spin-up were required to stabilise the numerical model and therefore they were excluded from the analysis.

The model solution was evaluated against different data sources. Modelled Sea Surface Temperature (SST) was compared to satellite-retrieved SST observations (reprocessed Pathfinder V5.3; CMEMS). The model tends to overestimate slightly the annual mean but otherwise, it captures well the spatial-temporal distribution, showing colder waters in coastal regions (due to upwelling) and warmer waters in open ocean regions for both the Gulf of Cádiz and the Alborán Sea (see Figure A.1). We also compared temperature-salinity (TS) diagrams using modelled outputs versus *in situ* observations from the Medatlas II dataset (http://www.ifremer.fr/medar/). The main water masses are well reproduced by our regional model as inferred from the TS diagrams (Figure A.2). Further details can be found in the supplementary material.

Finally, thermistors and Acoustic Doppler Current Profiler (ADCP) data collected in the proximity of Cape Trafalgar from September 3^{rd} to October 10^{th}, 2015 (MEGAN Project; Bolado-Penagos et al., 2020), were compared with model outputs to evaluate the tidal variability (Figure 2). The mooring was bottom-mounted at 6.05 °W – 36.00 °N (red cross in Figure 1b) at a bottom depth of 200 m. At this emplacement was deployed a thermistor chain of 43 thermistors disposed 3-m apart from each other, from 10 to 136 m depth and programmed with a sample interval of 1 minute. Additionally, it was also deployed a 75-kHz Teledyne RD Instrument (RDI) ADCP, with a sampling interval of 3 minutes and a 4-m bin size covering between 40 and 140 m of the water column. Because the model outputs represent a climatological year, to compare the observed and modelled data it was identified the closest tidal moment to the observations. Model data showed a temperature overestimation of 1.21 ± 0.64 °C (Figure 2a). Meanwhile, the current velocity data, uvel and vvel, range between very similar ranges. However, modelled uvel seems to slightly overestimate the observations (Figure 2b), while vvel seems to slightly underestimate them

(Figure 2c). Both tidal components, semi-diurnal and fortnightly, are well captured by the model allowing us to pursue the aim of this study.

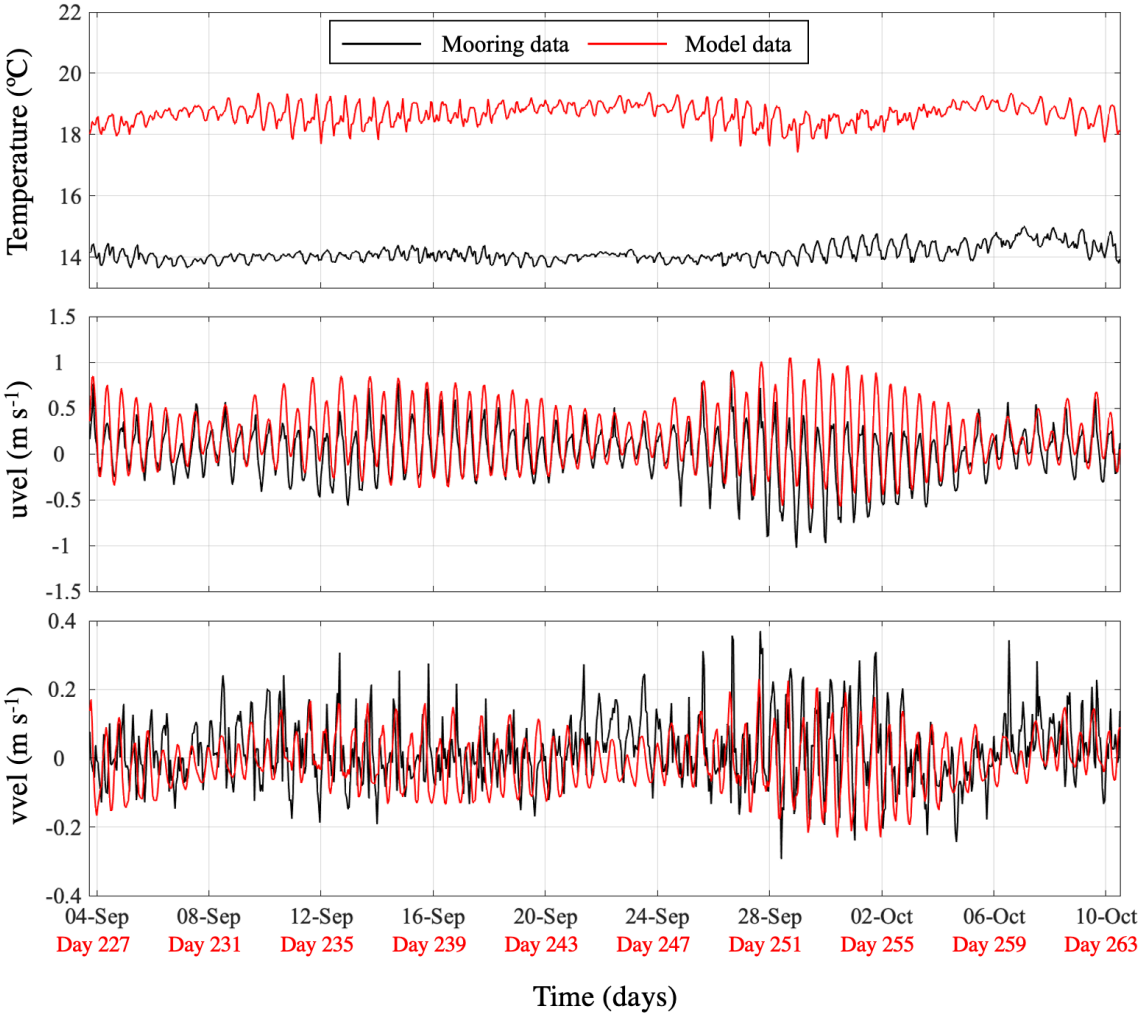

Figure 2: Temporal evolution of (a) mean temperature (°C), (b) mean zonal component of the current speed (uvel; m s^{-1}), and (c) mean meridional component of the current speed (vvel; m s^{-1}) for observed (black lines) and modelled (red lines) data. All time series were computed for the whole water column at 6.05 °W - 36.0 °N (red cross in Figure 1b). The x-axis labels show in black the sampled days of the mooring and the corresponding days of the model in red.

2.2. Ecosystem model

We used a simplified configuration of the Darwin model (version 1) that simulates the planktonic ecosystem (Follows et al., 2007; Dutkiewicz et al., 2009; Vallina et al., 2014a,b), being natively coupled to the MITgcm physical ocean model described above. Four phytoplankton functional groups are defined based on nutrient requirements and uptake strategies, with a transition from gleaners to opportunists: *Prochlorococcus*, *Synechococcus*, flagellates and diatoms (see Figure 2a in Vallina et al., 2017). All groups are limited by phosphate (PO_4), nitrate (NO_3), ammonium (NH_4) and iron, while diatoms are also limited by silicate (SiO_4). The model defines one generic zooplankton herbivore that feeds upon all phytoplankton species (killing-the-winner behaviour), and one generic zooplankton carnivore feeding on the

zooplankton herbivore acting as a closure trophic level for the food web. For a detailed description of the ecological model, the reader is referred to Vallina et al. (2014a,b). The model parameters are given in Table B.1.

Initial conditions for all the ecological tracers were based on a global model output from Vallina et al. (2014a). Phytoplankton initial conditions are the same for the four functional groups, applying the same biomass distribution. The same approach is used for zooplankton initial conditions. Boundary conditions were only prescribed for nutrients (PO_4, NO_3, NH_4, SiO_4) and phytoplankton biomass. Daily fields for the prescribed boundary conditions were derived from the IBI Biogeochemical Analysis and Forecast product from CMEMS (IBI-BIO). Phytoplankton boundary conditions were computed from the total biomass of the IBI-BIO model, using the same boundary condition for the four phytoplankton groups. These oceanic boundary conditions are only open for the prescribed tracers, so that those state variables with prescribed values at the boundary can leave the model domain through them. For those tracers for which there are not enough data at the boundary conditions, homogeneous Neumann boundary conditions (zero-flux) are applied (Sánchez-Garrido et al., 2015). Finally, at the sea surface, the model is forced with daily photosynthetically active radiation (obtained from ERA-Interim) and daily iron dust deposition (computed from modelled monthly data from Mahowald et al., 2003).

Due to the high computational cost of the hydrodynamic model (integration time-step of 15 seconds), the coupled biophysical model MITgcm + Darwin was run in offline mode (integration time-step of 240 seconds) using as physical forcing (inputs) the previously saved simulation (outputs) with the MITgcm hydrodynamic model on an hourly temporal resolution of temperature, salinity, vertical mixing, and velocity fields. Such a high temporal resolution (hourly) for the environmental variables was necessary to capture the tidally driven processes. The coupled biophysical model was run for 5 years, with 4 years of spin-up required to reach (quasi) steady-state seasonal cycles that were excluded from the analysis. Despite the relative complexity of our plankton model configuration and considering the aims of the study, we will only focus our analyses on the total phytoplankton biomass.

The seasonal variability of the ecosystem model was evaluated with satellite chl-*a* (mg m^{-3}) data, a proxy for the surface phytoplankton biomass. Ocean colour images for the study area were downloaded from the CMEMS (from 1998 to 2016). To enable this comparison, the model total phytoplankton biomass (mmol P m^{-3}) was first converted to carbon by applying the canonical Redfield ratio C:P = 106:1 (mol mol^{-1}), and then converted to chl-*a* concentration by applying a variable C:Chl ratio calculated as a function of light levels following Lefèvre et al. (2002) (see supplementary material for more details). Figure 3 shows the comparison between the seasonal climatology derived from remote sensing images and the model-derived seasonal average of the simulated year for surface chl-*a*. The modelled chl-*a* distribution reflects well the observed oligotrophic nature of the Western Alborán Gyre. Furthermore, the model also captures the meridional gradient of chl-*a* with higher values along the northern coast of the study area, as well as the decrease west-to-east of chl-*a* concentration in the Alborán Sea, being the north-western region the richest area (e.g., Sarhan et al., 2000; Macías et al., 2008). The under-estimation of chl-*a* concentration by our simulations over the northern coastal area of the Gulf of Cádiz may be attributed to the fact that the model does not prescribe nutrient inputs from river

discharges (e.g., Guadalquivir River; Huertas et al., 2005; Navarro et al., 2006).

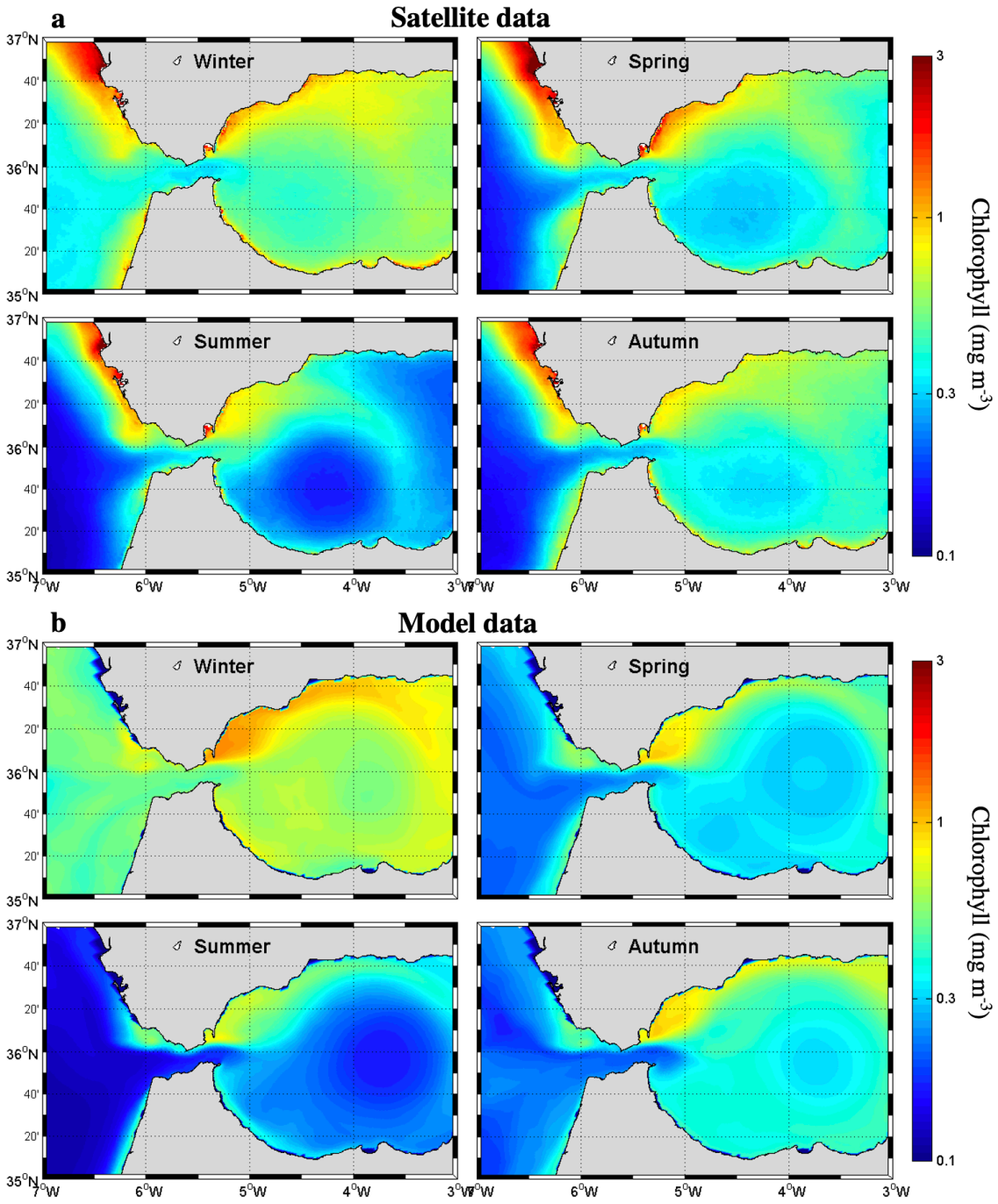

Figure 3: (a) Seasonal climatology of surface chlorophyll (mg m^{-3}) derived from remote sensing images corresponding to the period 1998 - 2016. (b) Model-derived seasonal climatology of surface chlorophyll (mg m^{-3}) for the 5^{th} year of simulation.

2.3. Wavelet analysis

Wavelet analysis is a powerful tool that allows a local time-scale decomposition of the signal in both time and frequency domains simultaneously (Lau and Weng, 1995; Torrence and Compo, 1998; Klvana et al., 2004; Cazelles et al., 2008). This tool is especially relevant for the analysis of non-stationary systems (see Cazelles

et al. (2008) for a review). Here, wavelet analysis is used to disentangle the temporal patterns of several state variables of the MITgcm + Darwin model, both in time and frequency domains. In particular, we use it to identify the dominant periodicities of salinity, temperature, NO_3 and phytoplankton biomass. We used the MatLab toolbox developed by Cazelles and Chavez (Cazelles et al., 2008), applying the Morlet wavelet that provides a good balance between time and frequency localisation (Grinsted et al., 2004). In a time-frequency plane, the wavelet power spectrum represents the relative importance of frequencies at each time step. Values closer to the edge of the time series, delimited by the cone of influence, were rejected to avoid false periodic events (Torrence and Compo, 1998). For each period, the average wavelet power spectrum was calculated, identifying the averaged variance contained in all wavelet coefficients of the same frequency. Furthermore, a 5% significance level was determined for WPS through a bootstrapping scheme using a hidden Markov model, to assess whether the wavelet-based quantities were due to just random processes (Cazelles and Stone, 2003).

Of particular interest is the fact that wavelet analysis allows the estimation of the coupling between driver and response variables, as well as the level of synchrony between them (Keitt and Fischer, 2006; Ménard et al., 2007; Buttay et al., 2017). The wavelet coherence analysis (WCo) was applied to analyse the synchrony between the zonal component of the current velocity (uvel; driver variable) and several model state variables: salinity, NO_3 concentration and phytoplankton biomass (response variables). Once identified the time scale at which the two non-stationary time series were locally linearly correlated, their phases, for this time scale, were extracted and compared (Cazelles et al., 2008). The phase difference between signals indicates whether or not they are in synchrony; and if they are not, the time lag between them.

3. Results

3.1. Spatial and temporal variability

For the simulated year, we evaluated the dynamics of salinity, temperature, NO_3 concentration, and total phytoplankton biomass along a (i) vertical two-dimensional section perpendicular to the submarine ridge (Barbate High) and parallel to the coast (black line in Figure 1b), and (ii) at the surface waters of the Trafalgar region (see the white box in Figure 1b). Due to the curvilinear grid of the model, we had to perform a data interpolation to properly show the vertical section. Thus, the values shown in the surface map (left-hand panels in Figures 5, 6, 7) do not always match exactly those shown along the vertical section (right-hand panels in Figures 5, 6, 7), but the general trend can be well appreciated.

The dynamics of the spatial distribution observed for the several tracers in the Trafalgar region show a temporal variability closely related to the tidal cycle. Therefore, in this particular subsection, we place the focus on the fortnightly tidal cycle that runs approximately from day 20 at 02:00 hours to day 34 at 20:00 hours. We can observe that the strongest tide-topography interaction in Barbate High takes place when the tidal current flows westward. This interaction is closely related to the intensity of the tidal current, being stronger at higher uvel values. Therefore, for the sake of simplicity, only the time of maximum tidal current towards the Gulf of Cádiz during neap and spring tides will be described (i.e., NT1 and ST1; Figure 4). The

time of maximum tidal current towards the Alborán Sea during neap and spring tides (NT2 and ST2, respectively) are shown in Figures D.1 to D.3. We will use salinity as a good upwelling indicator for this region.

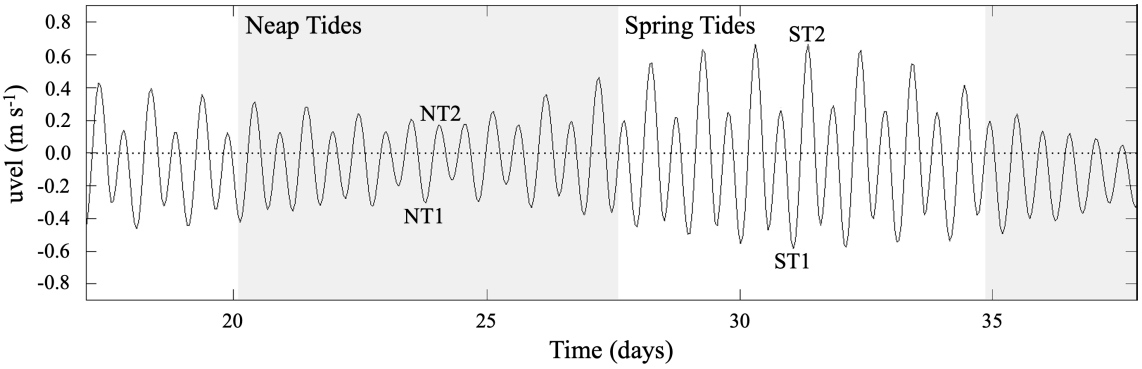

Figure 4: Temporal evolution of the mean zonal component of the current velocity (uvel; m s^{-1}), computed for the whole water column at 6.11 °W and 36.06 °N (red circle in Figure 1b), between days 17 and 38 of the simulated year. The black dashed line represents the zero reference, which delimits positive (negative) values that indicate flow driven eastward (westward), towards the Alborán Sea (Gulf of Cádiz). Points NT1 and NT2 indicate the examined neap tidal moments. Points ST1 and ST2 indicate the examined spring tidal moments. Grey background identifies neap tidal periods.

Figure 5 shows the vertical (left-hand panels) and the surface (right-hand panels) distribution of salinity in the Cape Trafalgar region. Both during neap and spring tides, along the vertical section parallel to the coast, we can observe a non-symmetric distribution of salinity determined by the presence of the submarine ridge (i.e., Barbate High), which has a steeper slope on its east side ($\sim$ 44%) than on its west side ($\sim$ 15%). However, during the neap tide period, this west-to-east asymmetry is less pronounced (Figure 5a). On the east side of the ridge, between 6.13 and 6.06 °W, we observe the highest salinity values (left-hand panels in Figure 5). This band of high salinity waters shows higher values at deeper layers than at the surface. During the spring tide, when the uvel towards the Gulf of Cádiz is maximum (- 0.58 m s^{-1}), the upwelling of saltier waters is most intense and reaches the most superficial layers of the water column ($\sim$ 36.50 - 36.80; Figure 5c). Meanwhile, during the neap tide (- 0.31 m s^{-1}), the upwelled water is less saline (coming from a shallower depth) and does not reach the most superficial layers ($\sim$ 36.40 - 36.50; Figure 5a). The surface distribution of salinity displays a tongue characterised by moderately high values relative to the surrounding waters, over and to the east of Barbate High (right-hand panels in Figure 5). The origin of this tongue is the region characterised by the band of high salinity waters observed in the vertical section (around the black circle) and its distribution is affected by the cyclonic eddy that develops due to the interaction of the westward tidal current with the eastern edge of Barbate High (see the black arrows in the right-hand panels in Figure 5). This eddy is more energetic (stronger horizontal mixing) during spring tides, leading to a less salty tongue ($\sim$ 36.45; Figure 5d) than during neap tides when it leads to a saltier tongue (weak horizontal mixing) ($\sim$ 36.40; Figure 5b).

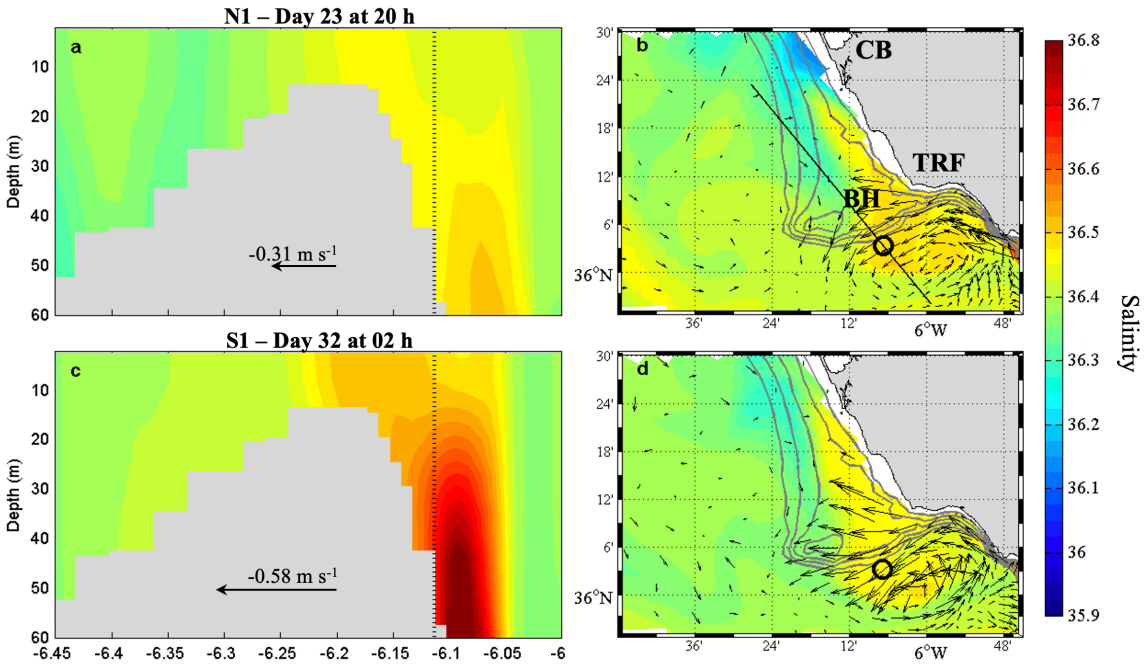

Figure 5: Salinity distribution in the Cape Trafalgar region during the maximum westward flow of the neap tide period (NT1: a, b) and the spring tide period (ST1: c, d) (see Figure 3). Left-hand panels show the vertical distribution along a section perpendicular to the submarine ridge (black line in panel b). Vertical dashed lines correspond to the position of open circles in the right-hand panels. Black arrows (a, c) represent the magnitude and direction of the mean zonal component of current velocity (uvel; m s^{-1}), computed for the whole water column at 6.11 °W and 36.06 °N at each time-step. Right-hand panels show the surface distribution. Black surface vectors represent the surface current (m s^{-1}). Grey solid lines represent the bathymetry (10, 20, 30, 40 and 50 m depth). BH: Barbate High. CB: Cádiz Bay. TRF: Cape Trafalgar.

During both neap and spring tides, NO_3 concentration along the vertical section parallel to the coast also displays a non-symmetric distribution (see left-hand panels in Figure 6). Maximum values, between $\sim$ 1.50 and 3.00 mmol m^{-3}, are found at the eastern side of the submarine ridge, mainly between 6.13 and 6.06 °W, concurrent with the band of high salinity values (see left-hand panels in Figure 5). Like salinity, this band of NO_3-rich water presents the highest concentration values in the deeper layers and during spring tides, when the intensity of the westward tidal current is stronger. However, in contrast to salinity distribution, there is not an east-to-west gradual decrease of NO_3 concentration since the lowest values are registered over the shallowest area of Barbate High ($<$ 1.00 mmol m^{-3}). The superficial distribution of NO_3, at both tidal moments, shows a spot of relatively high NO_3 concentration ($>$ 1.50 mmol m^{-3}) around the location of the band of NO_3-rich water observed in the vertical section (i.e., black circle on the right-hand panels in Figure 6). As with salinity, NO_3 surface distribution is affected by the cyclonic eddy. Thus, during neap tides, when the current speed in the cyclonic gyre is low resulting in a weaker horizontal dispersion, NO_3 concentration around the upwelling point is higher. Meanwhile, during spring tides, when the current speed in the gyre is higher, increasing the horizontal dispersion, NO_3 concentration around this point is lower. However, the presence of a NO_3-rich tongue is not as clearly defined as the salinity tongue over Barbate High. Moreover, along the coast from the Cádiz Bay to Barbate High, following the bathy-

metric lines, we observe a fringe with minimum NO_3 concentration values (< 1.00 mmol m^{-3}; Figure 6b, d).

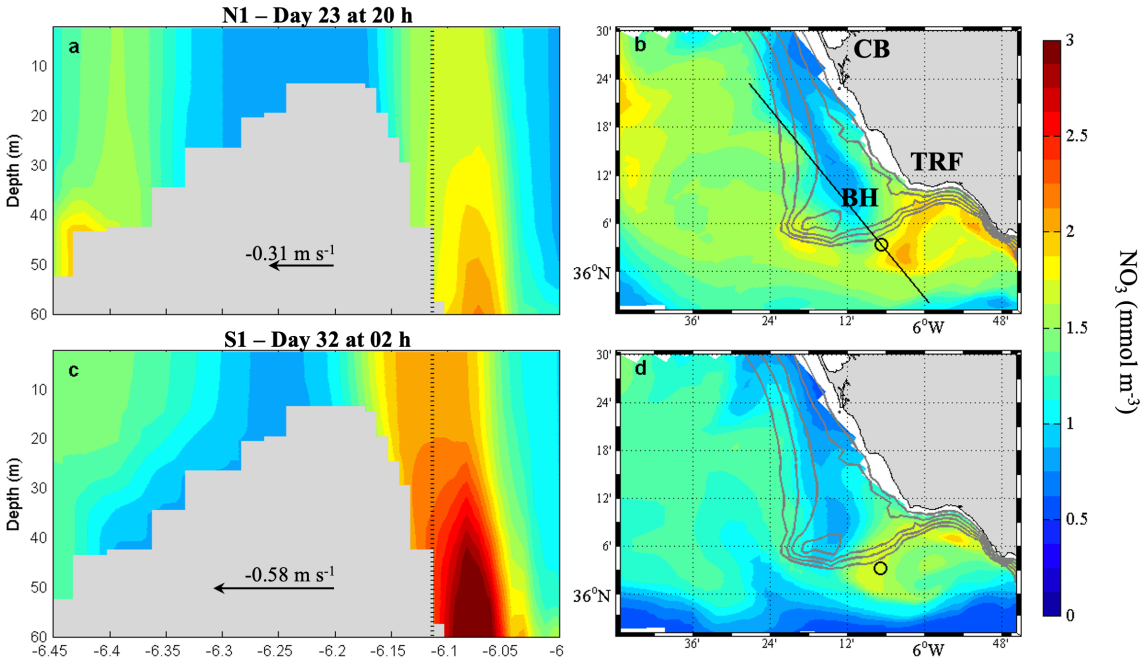

Figure 6: Nitrate concentration (NO_3, mmol m^{-3}) distribution in the Cape Trafalgar region during the maximum westward flow of the neap tide period (NT1: a, b) and the spring tide period (ST1: c, d) (see Figure 3). Left-hand panels show the vertical distribution along a section perpendicular to the submarine ridge (black line in panel b). Vertical dashed lines correspond to the position of open circles in right-hand panels. Black arrows (a, c) represent the magnitude and direction of the mean zonal component of current velocity (uvel; m s^{-1}), computed for the whole water column at 6.11 °W and 36.06 °N at each time-step. Right-hand panels show the surface distribution. Grey solid lines represent the bathymetry (10, 20, 30, 40 and 50 m depth). BH: Barbate High. CB: Cádiz Bay. TRF: Cape Trafalgar.

Total phytoplankton biomass distribution along the vertical section (see left-hand panels in Figure 7), shows a pattern quite different from the other state variables. During both neap and spring tides, maximum phytoplankton biomass values appear over the shallowest area of the ridge (> 0.70 mmol N m^{-3}). During neap tides, high biomass values are also observed in the most superficial layers of the water column to the east side of the ridge (Figure 7a). The vertical distribution of total phytoplankton biomass along the band between 6.13 and 6.06 °W, shows an opposite distribution to salinity and NO_3 concentration, showing low phytoplankton biomass in the recently uplifted waters (Figures 6 a, c and 6 a, c). Thus, low phytoplankton biomass is observed at the deeper layers where NO_3 concentration is maximum, progressively increasing to superficial layers at the same time that NO_3 concentration decreases (see left-hand panels in Figures 6 and 7). The surface distribution of total phytoplankton, at both tidal stages, shows a tongue over Barbate High characterised by high biomass (> 0.80 mmol N m^{-3}; see right-hand panels in Figure 7) displaced to the east side of the ridge due to the influence of the cyclonic eddy (Figure 7 b, d). This tongue is richer in phytoplankton biomass during spring tides (Figure 7d) when the input of NO_3-rich water is maximum (Figure 6 c). Moreover, phytoplankton biomass through

this tongue seems slightly higher close to the coastline extending from Cádiz Bay to Cape Trafalgar. Also, in the rest of the domain (mainly over the continental slope), phytoplankton biomass is higher during spring tides than during neap tides. This pattern is the opposite of the one observed for the NO_3 distribution, whose concentration over the continental shelf is slightly higher during neap tides than during spring tides (Figure 6 b, d).

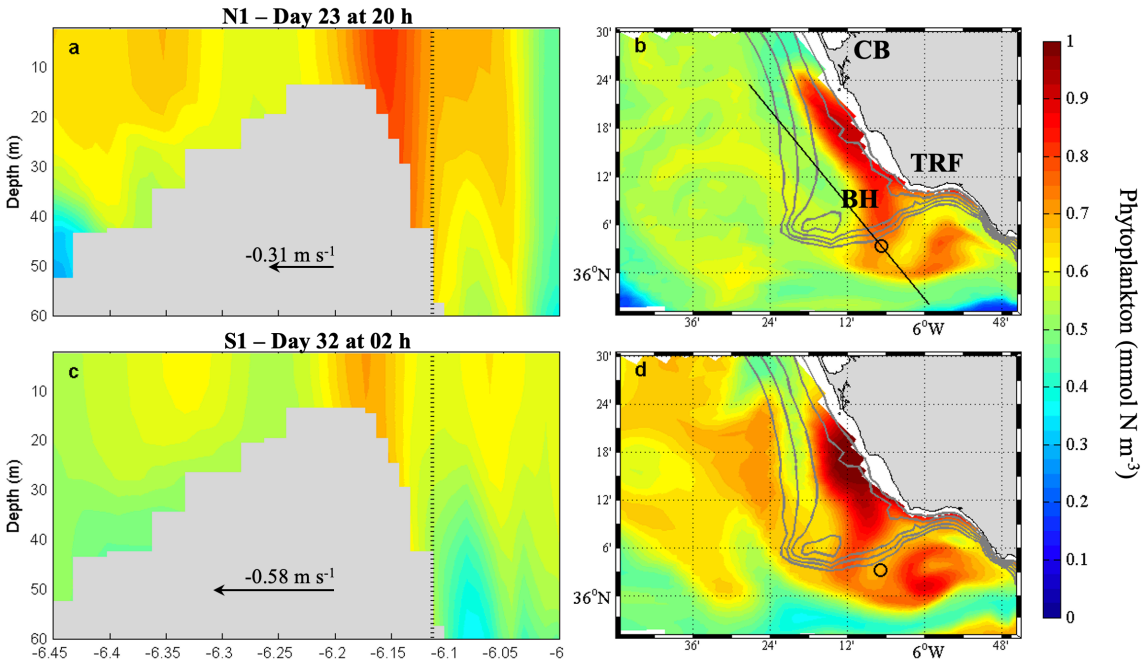

Figure 7: Total phytoplankton biomass (mmol N m^{-3}) distribution at Cape Trafalgar region during the maximum westward flow of the neap tide period (NT1: a, b) and the spring tide period (ST1: c, d) (see Figure 3). Left-hand panels show the vertical distribution along a section perpendicular to the submarine ridge (black line in panel b). Vertical dashed lines correspond to the position of open circles in right-hand panels. Black arrows (a, c) represent the magnitude and direction of the mean zonal component of current velocity (uvel; m s^{-1}), computed for the whole water column at 6.11 °W and 36.06 °N at each time-step. Right-hand panels show the surface distribution. Grey solid lines represent the bathymetry (10, 20, 30, 40 and 50 m depth). BH: Barbate High. CB: Cádiz Bay. TRF: Cape Trafalgar.

The sequential analysis of the vertical and superficial distribution of these three variables shows how the band of saltier, NO_3-rich and with low phytoplankton biomass water, as well as the cyclonic gyre and the tongue over Barbate High (and the surrounding waters), oscillate continuously from east-to-west due to the cyclical change of direction of the zonal component of the tidal current. Thus, the 'water masses' in the Trafalgar region are displaced to the east when uvel flows towards the Alborán Sea (positive values), and to the west when uvel flows towards the Gulf of Cádiz (negative values). Furthermore, these east-to-west-to-east oscillations are more or less noticeable depending on the intensity of uvel. To better observe this oscillating movement that is a consequence of the tidal cycle, and all its associated processes, the reader is referred to the supplementary video that shows the computer simulation of these variables for the first 3 months of the simulation (http://t.ly/bVQQ).

3.2. Hovmöller diagram

In the previous subsection, we described how an entry of saltier, nutrient-rich and low phytoplankton biomass water is observed between $\sim$ 6.13 and 6.06 °W, with a time-dependent variability closely related to the tidal cycle. To examine this process in more detail, in Figure 8 we show the Hovmöller diagrams (depth-variability as a function of time) of several state variables and R_i together with the temporal dynamics of uvel to outline the tidal cycle. We do so for a particular location at 6.11 °W - 36.06 °N (see the red circle in Figure 1b) and for the whole simulated year.

The time-dependent distribution of salinity shows a fortnightly periodicity. Higher values of salinity are observed during spring tides (Figure 8b). During the most intense spring tide periods (every $\sim$ 30-days) the water is slightly saltier than during the less intense periods, although in both cases the upwelled water always reaches the most superficial layers of the water column. Whereas during the neap tide periods (i.e., weak turbulent mixing) the lowest values of salinity are observed. It should be noted that for the entire period, the salinity of the water column continuously oscillates between relatively high and relatively low values, in good agreement with the tidal current oscillations both in direction and intensity. From July to November, the upwelling events seem to be less intense than during the rest of the year, with shallower (intermediate) and less salty upwelled water than that observed in other spring tide periods, probably North Atlantic Central Water (NACW), reaching the most superficial layers. Furthermore, from October to December we observe the lowest salinity values for the whole year of simulation.

The temperature at the selected location point also shows a pattern of variability associated with the fortnightly tidal cycle, although it is less appreciable than for salinity (Figure 8c). During spring tide periods, we observe the lowest water-column temperatures and highest salinity values (Figure 8b), the temperature is colder during the most intense spring tides. Conversely, during neap tides, the observed temperature is $\sim$ 2 °C warmer. As with salinity, the water temperature oscillates between relatively high and relatively low values depending on the tidal cycle. During the winter months (January to April), as expected, the coldest temperatures of the year are observed. While from July to November, in the first 30 m of the water column are observed the highest temperatures ($\sim$ 22 - 24 °C) of the whole year.

The seasonal variability of stratification and tides modulate the intensity of diapycnal mixing over the water column, as suggested by the Richardson number, $R_i = N^2/U_z^2$ reaches the greatest values from June to October associated to a strong summer thermocline that warrants flow stability ($R_i \gg 1/4$). During the rest of the year, the flow is also rather stable ($R_i > 1/4$), but with some small-scale potentially unstable patches of the fluid where vertical mixing is enhanced ($R_i < 1/4$. At fortnightly tidal scale, R_i shows smaller values (enhanced mixing) during spring tides. The fortnightly signal is especially noticeable during the summer months.

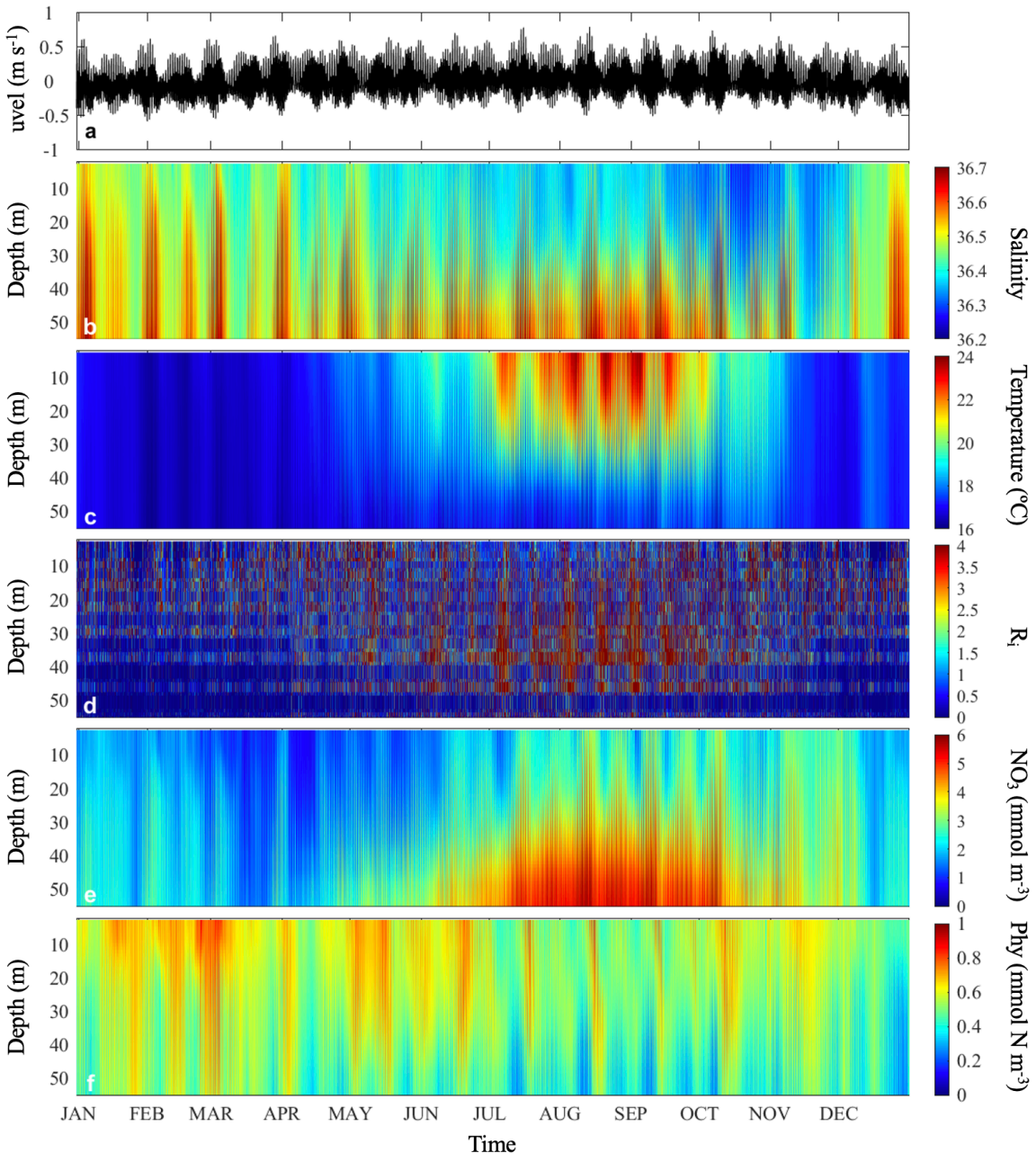

Figure 8: (a) Temporal evolution of the mean zonal component of current velocity (uvel; m s^{-1}), computed for the whole water column at 6.11 °W and 36.06 °N (red circle in Figure 1b), along the whole-year simulation. Hovmöller diagrams, computed at the same point (red circle in Figure 1b), illustrating spatial (i.e., depth) and temporal variability of (b) salinity, (c) temperature (°C), (d) the Richardson number (R_i, adimensional), (e) nitrate concentration (NO_3, mmol m^{-3}) and (f) total phytoplankton biomass (Phy, mmol N m^{-3}).

NO_3 concentration also displays a fortnightly periodicity (Figure 8e). Only during the most intense spring tides, NO_3-rich water seems to reach the surface layers. During neap tides, NO_3 concentration throughout the water column is relatively low ($<$ 1.00 mmol m^{-3}). As with salinity and temperature, the NO_3 concentration of the whole water column continuously alternates between relatively high and relatively low values, in agreement with the tidal current oscillations (direction and intensity).

Throughout the whole year, the lower NO_3 concentration values are observed from March to May (Figure 8e). While the maximum NO_3 concentrations are observed from July to October, coinciding with the period of highest stratification of the water column (Figure 8d). As a result, the nutrient-rich upwelled water is unable to reach the most superficial layers of the water column. The upwelling of less salty and nutrient-rich waters (compared with other upwelling events) supports the fact that during fall there is an upwelling of NACW in this region.

Figure 8f shows the dynamics of total phytoplankton biomass, with higher values at surface layers that tend to decrease with depth. Nevertheless, the phytoplankton biomass is quite high at all depths because the vertical domain analysed here is relatively shallow (50 m) and therefore well illuminated. As previously observed (Figures 5 and 6), phytoplankton biomass distribution behaves oppositely to NO_3 concentration. Thus, during the neap tide periods, when NO_3 concentration throughout the water column is relatively low, phytoplankton biomass shows high values with a pretty homogeneous distribution. For phytoplankton biomass is slightly more difficult to appreciate a fortnightly periodicity than for salinity, temperature or even NO_3 concentration. Although, as with the other variables, a continuous fluctuation between high and low phytoplankton biomass is still observed. Phytoplankton biomass is lowest from July to October when stratification is highest (Figure 8d), preventing them to access to the nutrient-rich upwelled water (Figure 8e).

3.3. Wavelet power spectrum

We performed a wavelet power spectrum analysis of the time series shown in the Hovmöller diagram to extract information about the temporal variability of salinity, temperature, NO_3 concentration and total phytoplankton biomass. The WPS was computed using the hourly average values for each variable using their averaged values for the water column.

The WPS for the salinity signal (time series) displays two strong peaks at $\sim$ 15-day and $\sim$ 30-day periodic components (Figure 9a). The time-averaged WPS shows that these two periodicities in the signal are statistically significant, contributing on average $\sim$ 21% and $\sim$ 31% of the total variance, respectively (Figure 9b). However, the $\sim$ 15-day WPS peak is statistically significant only during winter months, and the $\sim$ 30-day peak from January to mid-May and from October to December (Figure 9a). During the whole year, a second pair of peaks are observed at the $\sim$ 12-hour and $\sim$ 1-day periods (Figure 9a). For the $\sim$ 12-hour period, high values of WPS are observed during the most intense spring tides (i.e., approximately every 30 days), and weaker values during less intense spring tides. These discontinuous peaks of periodicities or frequencies in the WPS, disregarding the one observed (approximately) between days 15 and 23, are statistically significant. The peak in the $\sim$ 1-day periodicity shown by the WPS is almost coincident in time with the 12-hour period, although it is not always statistically significant. However, when looking at the time-averaged WPS, these two peaks (at $\sim$ 12-hour and $\sim$ 1-day) are small and therefore do not contribute significantly to the variance of the signal (Figure 9b).

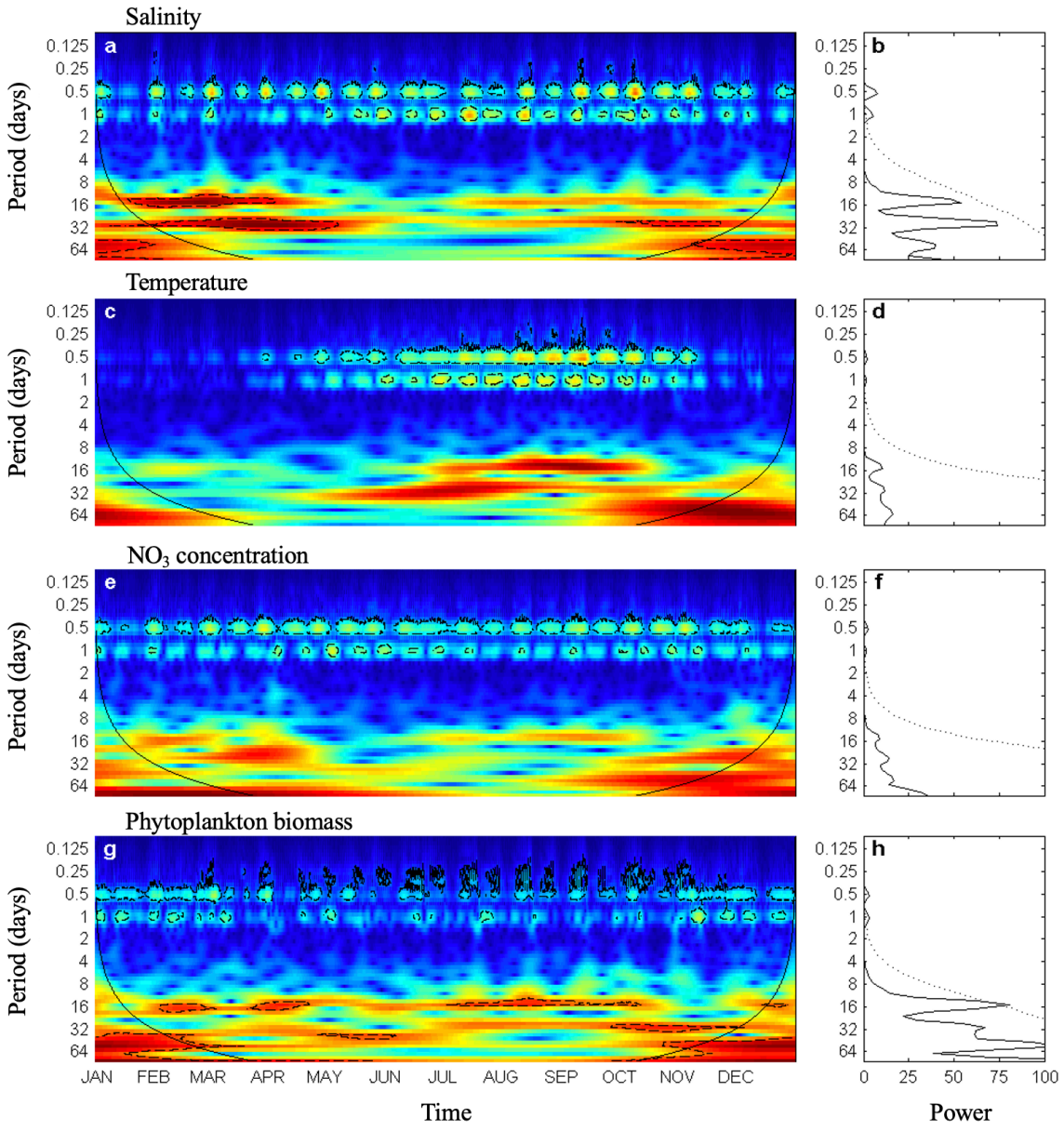

Figure 9: Wavelet analysis computed for the 1-year simulation. Left-hand panels: Wavelet power spectrum for (a) salinity, (c) temperature (°C), (e) nitrate concentration (NO_3, mmol m^{-3}) and (g) total phytoplankton biomass (mmol N m^{-3}). The colour code varies from dark blue (low values) to dark red (high values). Black lines indicate the cone of influence. Right-hand panels: Average wavelet power spectrum for (b) salinity, (d) temperature, (f) NO_3 concentration and (h) total phytoplankton biomass. Dotted lines, at all panels, show the $\alpha = 5\%$ significance level computed based on 1000 Markov bootstrapped series.

The WPS for temperature shows two relatively strong peaks at the $\sim$ 15-day and 30-day periodic components during the summer months, between June and October (Figure 9c). Both peaks, locally, are not statistically significant (i.e., time and period coordinates), although the time-averaged value of the WPS does highlight these periodicities as being statistically significant (Figure 9d). In particular, the $\sim$ 15-day periodicity of the temperature signal, although smaller compared to the one obtained for salinity, explains $\sim$ 26% of the total variance. From May to November, weaker but statistically significant peaks are observed for the 12-hour and 1-day periods (Figure

9c). Like salinity, the 12-hour periodicity peaks of temperature are slightly stronger during the events of most intense spring tides and weaker during less intense spring tides. The 1-day periodicity peak, which is weaker than the 12-hour peak, becomes relevant only during events of the most intense spring tides. Both time-averaged WPS peaks, 12-hour and 1-day, show low values not statistically significant.

The WPS for NO_3 concentration shows some strong but time-discontinuous peaks at the $\sim$ 15-day and $\sim$ 30-day periodic components of the signal, but locally they are not statistically significant (Figure 9e). However, the time-averaged WPS peaks for these signal periods are statistically significant. The observed peak at $\sim$ 15-day explains $\sim$ 12% of the total variance (Figure 9f). A weak time-discontinuous peak that is statistically significant can be observed at the $\sim$ 12-hour signal period (Figure 9e). This $\sim$ 12-hour peak shows slightly stronger values during the more intense spring tides and weaker during the less intense spring tides. At the $\sim$ 1-day periodic component, several peaks in the time domain are observed but only half of them are statistically significant. According to the time-averaged WPS, neither the $\sim$ 12-hour nor the $\sim$ 15-days periodic components are statistically significant (Figure 9f).

The WPS for total phytoplankton biomass shows a strong peak at $\sim$ 15-day periodic component, but its statistical significance is discontinuous in the time domain (from February to March, from mid-March to May, and from July to October; see Figure 9g). On average, this periodicity explains $\sim$ 21% of the total variance (Figure 9h). There are other strong peaks in the WPS between the $\sim$ 30-day and 60-day signal periods. As with previous state variables, weaker peaks are observed at $\sim$ 12-hour and $\sim$ 1-day periodicities, both discontinuous in time (Figure 9g). At the beginning and the end of the year, the 12-hour peak seems more uniform over time, without showing a discontinuous pattern as clear as for the other variables. The $\sim$ 1-day periodicity peak is slightly stronger and statistically significant at both the beginning and end of the simulated year. Between April and November, few of these peaks in the WPS at the $\sim$ 12-hour or $\sim$ 1-day signal periods are statistically significant. Furthermore, at the time-averaged WPS, both peaks were very weak and not statistically significant (Figure 9h). It should be noted that at several moments in the year, we can observe a peak in the WPS for the $\sim$ 6-hour signal period which is statistically significant, coinciding with the semi-diurnal tidal cycle.

3.4. Wavelet coherence analysis

Finally, we performed a wavelet coherence analysis to study the covariance between uvel as the driving variable and salinity, temperature, NO_3 concentration, and phytoplankton biomass as the response variables. The consistency of the coherence between the driver and the different response variables can be identified from the average wavelet cross-spectrum (see left-hand panels in Figure 10). The most consistent signal period for each pair of variables (i.e., the periodicity with the highest cross-spectrum power value) was identified, and subsequently, the corresponding oscillations were extracted for the whole period to compare their amplitudes and phases (see right-hand panels in Figure 10).

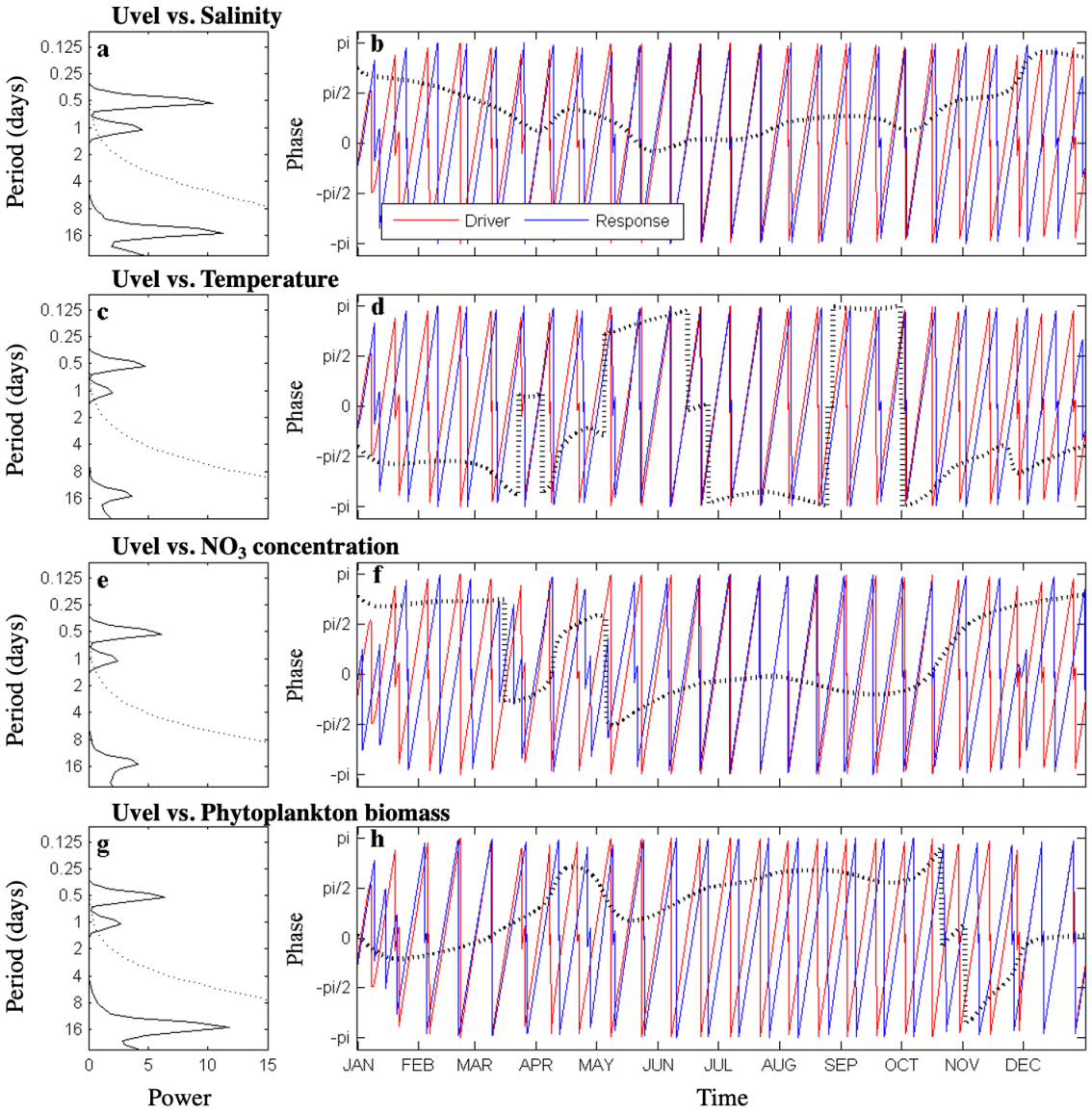

Figure 10: Wavelet coherence analysis computed for the zonal component of current velocity (uvel; m s^{-1}) versus (a, b) salinity, (c, d) temperature (°C), (e, f) nitrate concentration (NO_3, mmol m^{-3}), and (g, h) total phytoplankton biomass (mmol N m^{-3}) for the 1-year simulation. Left-hand panels (a, c, e, g) show the average wavelet cross-spectrum. Dotted lines show the $\alpha = 5\%$ significance levels computed based on 1000 Markov bootstrapped series. Right-hand panels show the phases of both time series computed for the peak of highest coherence: uvel (red line) versus (b) salinity, (d) temperature, (f) NO_3, and (h) total phytoplankton biomass (blue lines). Dashed lines represent the phase difference between both signals.

The strongest phase coherence between the uvel and salinity signals is found at the $\sim$ 15-day period, with a cross-spectrum power value that explains $\sim$ 37% of the total variance (Figure 10a). For the entire simulation, there is an average delay of 1.05 days between the phase of the two variables, with the driver variable (uvel) peaking before the response variable (salinity) (Figure 10b). The maximum delay between uvel and salinity signals is observed at the beginning and the end of the year, with a delay of 2.36 and 2.84 days, respectively, between driver and response. While the minimum delay is observed from June to August.

Between uvel and temperature, the strongest peak in the WCo analysis is observed at the $\sim$ 12-hour period (Figure 10c), although the area under this peak is not statistically significant. Therefore, as we did with salinity, we focus our analysis on the $\sim$ 15-day signal period. This peak has a power value that explains the $\sim$ 32% of the total variance. During most of the simulated year, the response variable (temperature) appears before the driver variable (uvel), with an average delay of 1.97 days (Figure 10d). However, between May and July and between September and October, the driver variable appears before the response variable, with a delay of up to 3.14 days.

The coherence between uvel and NO_3 concentration also shows the strongest and statistically significant peak at the $\sim$ 15-day period (Figure 10e). The $\sim$ 15-day cross-spectrum power value explains $\sim$ 23% of the total variance. Again, driver and response variables show a lack of synchrony (Figure 10f), with the response variable appearing before or after the driver. At the beginning and the end of the year, the driver (uvel) appears before the response (NO_3 concentration), with a mean delay of 2.27 days. From May to October, the response variable appears before the driver, with a mean delay of $\sim$ 0.50 days.

Likewise, total phytoplankton biomass displays the strongest coherence with uvel at the $\sim$ 15-day signal period, with a cross-spectrum power value that explains $\sim$ 48% of the total variance (Figure 10g). The delay between both variables follows a pattern almost opposite to uvel and NO_3 concentration (Figure 10f). The response variable appears before the driver at the beginning and the end of the simulated year, with a mean delay of 0.71 days. While from April to October, the driver variable appears before the response variable, with a mean delay of 1.38 days (see Figure 10h).

To verify that these results are not a consequence of our approach, both the WPS and the WCo analyses were repeated using two different time series: (i) a time series that only considers the temporal dynamics of salinity, NO_3 concentration and phytoplankton biomass at 20 m depth at 6.11 °W - 36.06 °N (red circle in Figure 1b); and (ii) a time series obtained from the average values, of each variable, for the whole water column and considering the entire upwelling band region, i.e., between 6.13 and 6.06 °W. In both cases, the obtained results were similar to those described here (data not shown).

4. Discussion

In the Cape Trafalgar region, the tide-topography interaction of the westward tidal current (towards the Gulf of Cádiz) with the eastern steep edge of the submarine ridge, results in a tidal pumping process that brings up deep, saltier, colder, nutrient-rich and phytoplankton-poor water onto Barbate High. This process is similar to the interaction previously described at Georges Bank, a shallow submarine feature located on the Gulf of Maine (e.g., Chen and Beardsley, 1998; Franks and Chen, 2001; Hu et al., 2008; Ji et al., 2008). Particularly during spring tides, denser water is advected upslope to subsurface layers leading to a spatial asymmetry between the eastern and the western side of the ridge (see left-hand panels in Figures 5-7) (Vargas-Yáñez et al., 2002). Concurrently, the interaction of the tidal current with the eastern edge of Barbate High leads to the formation of a cyclonic eddy (Bolado-Penagos et al., 2020), which spreads the upwelled waters over and to the west of the

ridge. This interaction results in the development of a water tongue with particular properties that are slightly different from the surrounding waters (right-hand panels, Figures 5-7). The upwelling of deep, salty and nutrient-rich water is more effective during spring tides, but due to the greater horizontal mixing mediated by the cyclonic gyre the water properties of are diluted, while during neap tides the lower horizontal mixing leads to a saltier and enriched water tongue.

The high phytoplankton biomass observed over Barbate High (right-hand panels in Figure 7), is favoured by the continuous and cyclical input of nutrients (e.g., Chen and Beardsley, 1998; Hu et al., 2008; Ji et al., 2008; Blauw et al., 2012, 2018). Actually, a previous study with a similar model configuration (Sánchez-Garrido et al., 2015) shows how a simulation with tidal forcing results in a chl concentration over Barbate High $\sim$ 3 times higher than in a simulation without tides. At the selected location point for in-depth analysis of the upwelling dynamics, we observe that NO_3 concentration and phytoplankton biomass display an anti-phase behaviour (Figure 8d, e). The 'water masses' observed in this region (i.e., Trafalgar's tongue, upwelled water) are continuously moving back and forth due to the fluctuations of the tidal current intensity and direction (see Supplementary video – http://t.ly/bVQQ). The pumping of NO_3-rich waters takes place when the tide flows towards the Gulf of Cádiz while Trafalgar's tongue moves westward. Hence, at the analysed upwelling point there is an uplifting of nutrient-rich water with relatively low phytoplankton biomass and a low influence of the phytoplankton-rich Trafalgar's tongue. Nevertheless, when the tide flows towards the Alborán Sea, there is no pumping of nutrient-rich water and the phytoplankton-rich Trafalgar's tongue is advected eastwards on the analysed upwelling point, and re-distributed along the whole water column. This coincides with a maximum in phytoplankton biomass. This fact can be appreciated in Figure 11a, where mean NO_3 concentration and phytoplankton biomass computed for the whole water column at the upwelling point (red circle in Figure 1b) over two tidal cycles behaves oppositely.

The tide-topography interaction occurs during both neap and spring tides (Figures 5 and 6). However, during neap tides the water advection is weak, so the pumped waters (slightly more saline and moderately rich in NO_3 than the surrounding waters) do not reach the most superficial waters (Figure 8c). The intensity of the tidal pumping of saltier, colder and NO_3-rich waters depends on the tidal current speed, being stronger and reaching the most superficial layers when the westward current speed (towards the Gulf of Cádiz) is higher (Figures 5, 6, 8 b-d). In Figure 8 b-d, it can be observed that the tidal pumping of saltier, colder and NO_3-rich waters takes place several days before uvel achieves its maximum speed during spring periods; when the tidal current speed is strong enough to cause a significant upwelling of deep waters. Figure 11b shows the temporal dynamics of the average uvel (m s^{-1}) and salinity, computed for the whole water column at 6.11 °W - 36.06 °N (red circle in Figure 1b) over two tidal cycles. It should be noted that the semi-diurnal tidal cycle in Trafalgar, with two high tides and two low tides per day, shows a diurnal inequality with one high-low tidal cycle more intense than the other. It also should be noted that during a semi-diurnal tidal cycle, due to the expected time delay between the maximum westward current flow (negative uvel) and the horizontal displacement of the water mass (high tide), the maximum upwelling of salty waters is observed 2 - 3 hours after the maximum flow. Thus, each peak of maximum salinity is caused by

the previous peak of maximum westward tidal current (towards the Gulf of Cádiz). Moreover, due to the diurnal inequality, the oscillations of salinity peaks are also asymmetric.

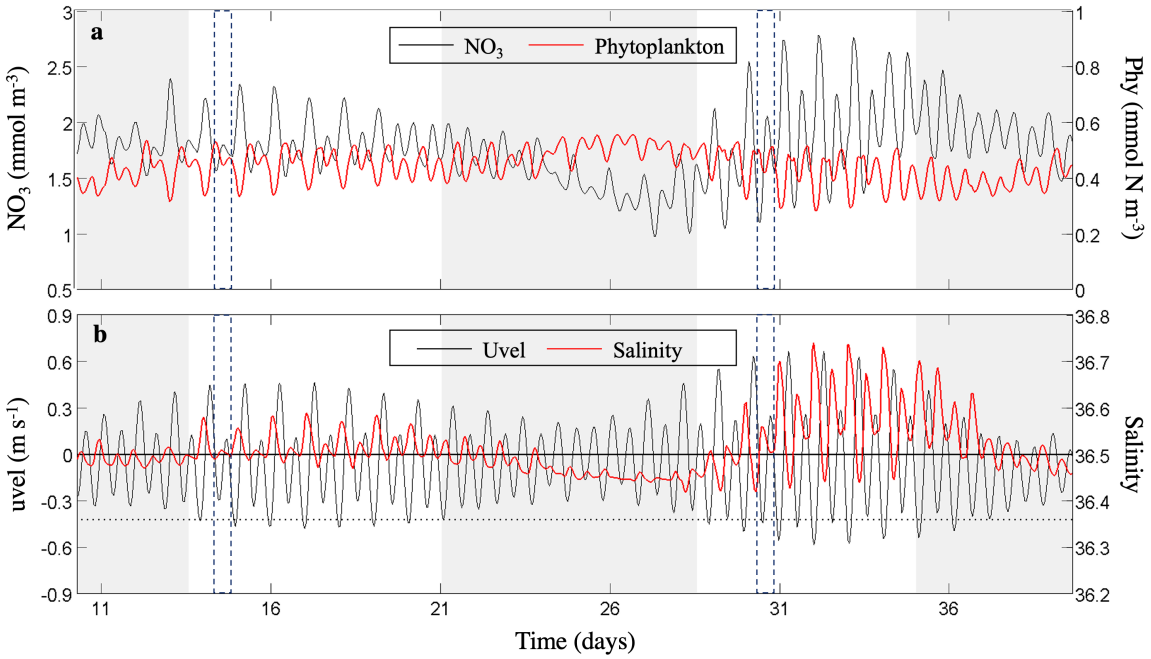

Figure 11: (a) Temporal evolution of mean nitrate concentration (NO_3, mmol m^{-3}; black line) versus mean phytoplankton biomass (Phy, mmol N m^{-3}; red line). (b) Temporal evolution of the mean zonal component of the tidal current (uvel, m s^{-1}; black line) versus mean salinity (red line). The black horizontal line represents the zero uvel reference (delimiting positive (negative) values that indicate flow driven eastward (westward), towards the Alborán Sea (Gulf of Cádiz)) and the mean salinity (36.47) value computed for the whole year. The black dashed line represents uvel equal to -0.42 m s^{-1}. Black dashed rectangles point out the first tidal-pumping event during both spring tide periods. The grey background identifies the neap tide periods. All time series were computed for the whole water column at 6.11 °W - 36.06 °N (red circle in Figure 1b).

Considering Figure 11b, it seems that the upwelling of saltier waters does not take place when the westward tidal current speed is lower than 0.42 m s^{-1} (negative uvel values, black dashed line). Black dashed rectangles mark the first effective tidal-pumping event during both spring tide periods. During the less intense spring tide, the first tidal-pumping event of deep and saltier water towards the more superficial layers occurs around day 13 at 02:30 hours, raising the average salinity to 36.58. Three hours before (around day 12 at 23:36 hours), the westward uvel is $\sim$ 0.42 m s^{-1}. In the previous days, characterised by lower uvel values, the upwelling of deep and saltier water does not take place. Similarly, during the most intense spring tide event, the first tidal-pumping episode takes place around day 29 at 03:48 hours, as a result of uvel $>$ 0.42 m s^{-1} (around day 29 at 01:54 hours). This behaviour is observed throughout the whole year (data not shown). However, this dynamic is influenced by the summer stratification of the water column (Figure 8d) linked with the seasonal variability of solar irradiance (and thus heat flux). In summer, although during spring tides the upwelling of salty and nutrient-rich waters continues to take place (Figure 8b-e), the heat-flux induced stratification reduces the vertical mixing preventing the upwelled waters from reaching the most superficial layers (Figure 8d).

Hence, the phytoplankton located in the most superficial layers will not have access to the uplifted nutrients, decreasing the phytoplankton community nutrient uptake rate and biomass (Figure 8f). This seasonal variability was preiously observed in the study region using 10-years of ocean colour observations using the MEdium Resolution Imaging Spectrometer ($\sim$ 300 m resolution Sala et al., 2018).

For all the analysed variables, salinity, temperature, NO_3 concentration and total phytoplankton biomass, the time-averaged WPS shows a peak at the fortnightly tidal cycle, explaining $\sim$ 21%, $\sim$ 26%, $\sim$ 12% and $\sim$ 21% of the total variance respectively (right-hand panels in Figure 9). Although the time-averaged WPS peak observed at the $\sim$ 15-day signal period for temperature is smaller than for salinity, it explains a higher percentage of the total variance (Figure 9d). However, the local WPS analysis shows statistically significant results for salinity at certain time periods of the simulated year but not for temperature (Figure 9 a and c), confirming that temperature is not a good proxy to identify tidally driven upwelling events in this region. Salinity and temperature are intrinsic properties of the upwelled water, and no biological activity can alter them. However, upwelled nutrients may be assimilated by phytoplankton, weakening the fortnightly periodicity component of NO_3 concentration, which would explain the absence of statistically significant peaks in the WPS analysis (Figure 9e). Furthermore, the lack of a statistically significant fortnightly periodicity component may also be related to the lack of continuity in the upwelling events, which are less intense during neap periods (Figure 8). In fact, the WPS analysis with daily averaged time series results in stronger fortnightly signals, statistically significant over longer periods (data not shown). Supporting these findings, the WCo analysis between state variables (drivers against responses) identifies the strongest statistically significant covariation patterns at the fortnightly tidal period (see left-hand panels in Figure 10). However, only in very few certain moments of the temporal domain, the driver variable (uvel) is in synchrony with the response variables (i.e., salinity, temperature, NO_3 concentration and total phytoplankton biomass). For most of the year, the time delay between driver and response variables varies back and forth. Although the tidal-topography interaction is the main responsible for the temporal and spatial variability in the Trafalgar region, it is not until the westward uvel reaches a threshold value of $\sim$ 0.42 m s^{-1} that deep water is pumped to the most superficial layers. Moreover, the tidal cycle is also responsible for the horizontal displacement of water masses that modifies the properties of the water column. Finally, the seasonal variability, the Gulf of Cádiz circulation pattern, and the wind regime will also introduce changes (Vargas-Yáñez et al., 2002; Sala et al., 2018). Therefore, this asynchrony between driver and response variables is conceptually expected but difficult to anticipate before performing the simulations, due to non-linearities in the dynamics.

The WCo analysis between uvel (as driver variable) against NO_3 concentration and phytoplankton biomass (as response variables) shows an opposite pattern (disregarding May) (Figure 10 f, h). When NO_3 oscillations appear later than the driver, the phytoplankton biomass oscillations appear earlier than the driver, and vice versa. In any case, the maximum of phytoplankton biomass must be a response to the previous NO_3 tidal pumping. This is explicit in the primary production equations of the ecosystem model used to perform these simulations. In the Cape Trafalgar region, there seems to be always a phytoplankton community ready to assimilate nutrients when there is a new input. After a neap tide period with a minimum nutrient input

(Figures 6c, 8c), during which the previously pumped nutrients have been consumed or dispersed, a new nutrient input during spring tides (when westward uvel > 0.42 m s^{-1}) can be efficiently assimilated by the pre-existing phytoplankton community. In fact, some modelling exercises have shown how patterns of periodic inputs of nutrients into the surface (especially tidal pulses) lead to the apparition of larger values of phytoplankton biomass than scenarios associated with a continuous supply; furthermore, it can favour some taxonomic groups as diatoms and larger zooplankton (Macías et al., 2010).

Although the fortnightly period is shown to be the most influential scale of the tidal variability in our study area, as previously found by Sala et al. (2018), it should be highlighted that the WPS and WCo analyses show a peak at the $\sim$ 12-hour period which confirms the influence of the semi-diurnal tidal cycle on the simulated state variables (see Figure 9 and left-hand panels in Figure 10). However, the time-averaged WPS and WCo analyses for the entire year show that this periodicity is not statistically significant, probably due to the discontinuity of the tidal-pumping events, which do not take place when uvel was < 0.42 m s^{-1}.

Previous studies have highlighted that the tidal pumping of nutrient-rich waters could be enhanced by other mechanisms not addressed in our study, such as river discharges (Huertas et al., 2005; Navarro et al., 2006) and wind-driven upwellings (Vargas-Yáñez et al., 2002; Sala et al., 2018). Our model configuration does not include nutrient inputs from river discharges (e.g., Guadalquivir River). This fact facilitates the aim of this study by removing its possible influence on the time series analysis. However, the lack of nutrient river discharges results in an underestimation of primary production of the northern coastal areas in the Gulf of Cádiz, which can be observed in Figure 3. The superficial circulation pattern of the Gulf would advect the productive water that flow from the rivers towards the Trafalgar region, increasing its primary production. Therefore, it would be interesting for future works to compare our results with a model that prescribes nutrient inputs from rivers to evaluate and quantify their relative importance. Regarding the wind forcing, since it was explicitly resolved in our model, we have extracted the zonal component of the wind at 10 m (u10) for the analyzed area. The comparison between both u10 and salinity time series does not show a clear pattern of variability (Figure E1), and the lack of correlation was supported by a WCo analysis (data not shown). Nevertheless, its influence may introduce 'noise' in our analysis but, as the seasonal variability, without undermining the tidal impact in the region. However, Bolado-Penagos et al. (2020) observed that easterly winds increase the retention capacity of Cape Trafalgar. Moreover, due to the presence of the ridge that characterizes this region a stacking of waters may take place leading to a deepening of the interface. Therefore, it would be interesting to carry out a more detailed analysis with a different model setup.

Finally, it is worth mentioning that several authors have described a secondary impact of the tidal cycle in the Strait of Gibraltar that would increase the primary production in the Alborán Sea. Due to the velocity divergences developed in the surface layer when undulatory features are generated over the Camarinal Sill, a lateral advection of patches with high chl-*a* concentration was observed from coastal areas to the centre of the Strait (Macias et al., 2006; Vázquez et al., 2009; Ramírez-Romero et al., 2012; Bruno et al., 2013). Thus, Cape Trafalgar is considered to act

as a source of nutrient- and biomass-rich waters that periodically will flow to the Alborán Sea. Moreover, a recent study (Bolado-Penagos et al., 2020) has described a transport process of phytoplankton along the coastal margin between Cape Trafalgar and the Alborán Sea. These transport events would imply a loss of nutrient and phytoplankton-rich waters towards Alborán that could be introducing some degree of 'noise' in our wavelet analysis (WPS and WCo).

5. Conclusions

The results obtained in this study confirm the importance of the tidal cycle for the productivity of the Cape Trafalgar region through an active and periodic forcing resulting in a pulsating upwelling pattern. The interaction of the westward tidal current with the eastern edge of the ridge perpendicular to the coast that characterises this region results in the upwelling of deep, saltier and nutrient-rich waters that favour the development of a tongue with high phytoplankton biomass over Barbate High.

The fortnightly period is confirmed as the most influential scale of the tidal cycle when the tidal-pumping process takes place during spring tides characterised by a westward tidal current > 0.42 m s^{-1}, between ~ 3 days before and after the moment of maximum westward flow. This tidal interaction implies cyclical fertilisation of the illuminated surface waters in the region, favouring the growth of the phytoplankton community. After an (effective) tidal-pumping event during spring tides, periods of minimum NO_3 concentration lead to phytoplankton nutrient-limitation at the surface and low primary production. However, these periods do not last long (~ 4 days).

The seasonal variability of solar radiation affects the Cape Trafalgar region only during summer. From July to September, the stratification of the water column increases the vertical thermal gradient in the water column, which decreases the vertical uplifting of nutrient-rich water into the first 30 m of the water column. For this reason, the upwelled nutrients driven by the tidal-topography interaction remain unconsumed below the euphotic layer, doubling their concentration by accumulation. Meanwhile, the phytoplankton biomass decreases due to a lower input of nutrients to the most superficial layers.

Acknowledgements

The model computations were conducted in the facilities of the 'Area de Sistemas de Información de la Universidad de Cádiz' (https://supercomputacion.uca.es/). Iria Sala thanks Juan C. González Cerezo for his technical support with the computational procedures. The authors thank CMEMS, ECMWF and IFREMER services for the distribution of the different datasets used in this work. The Spanish National Research Plan through project CTM2013-49048 has supported this work. Iria Sala and Marina Bolado-Penagos were supported by a grant from the FPI fellowship program. Part of this work was supported by national research grant CGL2013-41256-P (MARES) from the Spanish government to Sergio M. Vallina. To accomplish this work Iria Sala carried out one visiting research stay at the Institute of Marine Sciences (ICM – CSIC; Barcelona, Spain) under the supervision of Sergio M. Vallina and another visiting research stay at the Laboratoire d'Océanographie et du Climat (LOCEAN-UPMC; Paris, France) under the supervision of Dr Marina Lévy. These visiting

research stays were supported by PhD secondment grants from the FPI fellowship program.

Author contributions

Iria Sala: Conceptualization, Methodology, Validation, Formal analysis, Investigation, Data curation, Visualization, Writing – original draft, Writing – review and editing. **Sergio M. Vallina**: Conceptualization, Methodology, Validation, Formal analysis, Data curation, Supervision, Writing – review and editing. **Marina Lévy**: Supervision, Writing – review and editing. **Marina Bolado-Penagos**: Validation, Writing – review and editing **Carlos M. García**: Conceptualization, Funding acquisition, Project administration, Writing – review and editing. **Fidel Echevarría**: Conceptualization, Funding acquisition, Project administration, Writing – review and editing. **José C. Sánchez-Garrido**: Methodology, Formal analysis, Data curation, Supervision, Writing – review and editing.

Conflicts of interest

The authors declare no conflict of interest.

AppendixA. Validation of the circulation model

Sea Surface Temperature (SST). SST data for the study area and the period 2001 - 2010 were downloaded from the Copernicus Marine Environmental Monitoring Service (CMEMS; http://marine.copernicus.eu/). This product is based on the reprocessed Pathfinder V5.3 (PFV53) Advanced Very-High-Resolution Radiometer (AVHRR) data combined with a bias-corrected version of the CMEMS-NRT-L4 data, using an Optimal Interpolation algorithm to provide a full-time series of consistent daily gap-free maps with a resolution of $\sim$ 4.63 km.

Figure A.1 shows the comparison between the measured and modelled annual climatological values of SST. The climatological SST distribution is similar in both satellite data and the model, with colder coastal waters and warmer open ocean regions at both the Gulf of Cádiz and the Alborán Sea. Furthermore, it should be highlighted the presence of colder waters in the coastal region of Trafalgar, our area of interest. However, the model overestimates the annual mean satellite SST by $\sim$ 2 °C.

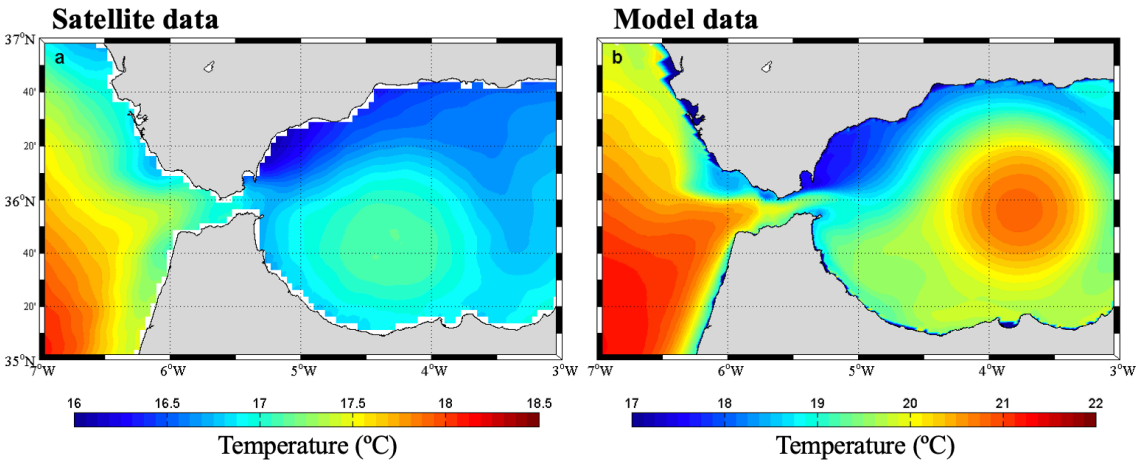

Figure A.1: (a) Sea surface temperature (SST, $^{-1}$C) climatology derived from remote sensing images corresponding to the period 2001 - 2010. (b) Model-derived climatology of SST for the 3^{rd}-year simulation. Please note the different ranges of the scale between both subplots.

Temperature-salinity diagrams. Temperature and salinity data for the study area were extracted from the Medar/Medatlas II project, whose objective is to make available a comprehensive data product of temperature, salinity and biochemical data in the Mediterranean and the Black Sea, through wide cooperation of the Mediterranean countries (http://www.ifremer.fr/medar/). Temperature and salinity data were collected from 1911 to 1987. Temperature-salinity diagrams were computed for the centre of both sub-basins, the Gulf of Cádiz and the Alborán Sea, from observed and modelled data (Figure A.2). The main water masses present in both sub-basins were quite well reproduced by our regional model (grey points).

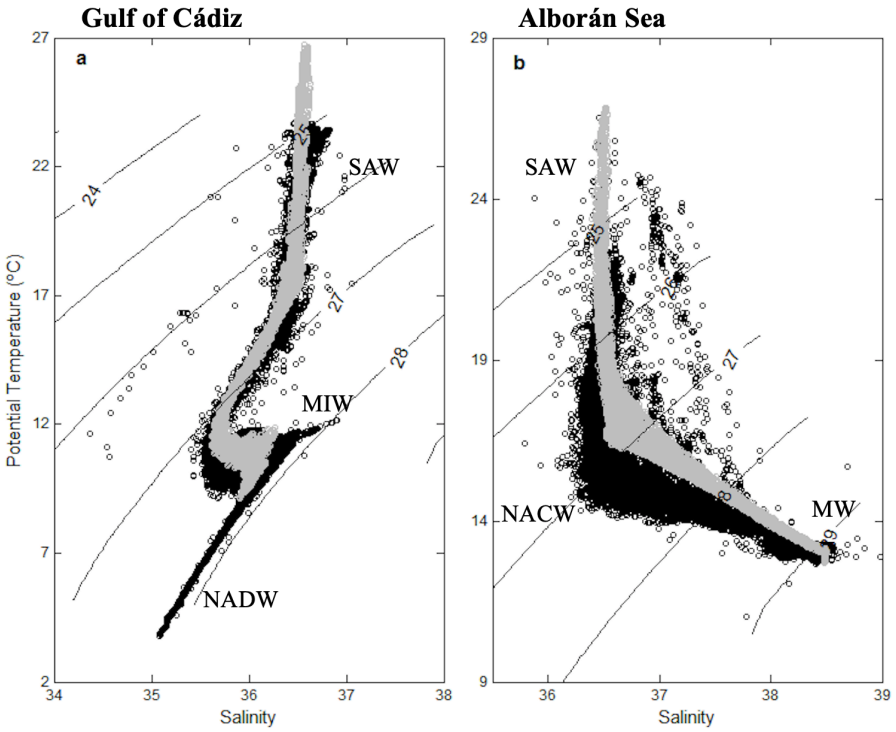

Figure A.2: Temperature-salinity diagrams comparing the Medatlas II database (black points) with the model outputs (grey points), representing the water mass characteristics of the (a) Gulf of Cádiz region, and the (b) Alborán Sea region. MIW: Mediterranean Intermediate Water. MW: Mediterranean Water. NACW: North Atlantic Central Water. NADW: North Atlantic Deep Water. SAW: Superficial Atlantic Water.

AppendixB. Ecosystem model: Ecological parameters

Table B.1: List of ecological model parameters. The values are shown in units of nitrogen. The corresponding values for phosphorus, silica and iron can be derived using a Redfield N:Si:P:Fe ratio of 16:16:1:0.001 (mol mol^{-1}). Dia.: Diatoms. DIM: dissolved inorganic matter. Din.: Dinoflagellates. DOM: dissolved organic matter. Mes.: Mesozooplankton. Mic.: Microzooplankton. n.d.: no dimensions. Phy.: Phytoplankton. POM: particulate organic matter. Pro.: *Prochlorococcus*. Syn.: *Synechococcus*. Zoo.: Zooplankton.

Parameter		Symbol	Value	Units
Phy. Pro.	Max. specific growth rate	μ_{max}^{pro}	0.50	d^{-1}
Phy. Syn.	Max. specific growth rate	μ_{max}^{syn}	1.00	d^{-1}
Phy. Fla.	Max. specific growth rate	μ_{max}^{fla}	2.00	d^{-1}
Phy. Dia.	Max. specific growth rate	μ_{max}^{dia}	4.00	d^{-1}
Phy. Pro.	Half-sat. for DIM uptake	ks^{pro}	0.10	μM
Phy. Syn.	Half-sat. for DIM uptake	ks^{syn}	0.30	μM
Phy. Fla.	Half-sat. for DIM uptake	ks^{fla}	0.60	μM
Phy. Dia.	Half-sat. for DIM uptake	ks^{dia}	1.20	μM
Phy.	Assim. efficiency	β_{phy}	0.80	n.d.
Phy.	Mortality specific rate	m_{phy}	0.05	d^{-1}
Phy.	Mortality fraction to POM	ω_{phy}	0.50	n.d.
Phy.	Non-assim. fraction to POM	ψ_{phy}	0.50	n.d.
Zoo. Mic.	Max. specific ingestion rate	g_{max}^{mic}	4.00	d^{-1}
Zoo. Mes.	Max. specific ingestion rate	g_{max}^{mes}	2.00	d^{-1}
Zoo. Mic.	Half-sat. for ingestion	kg^{mic}	0.50	μM
Zoo. Mes.	Half-sat. for ingestion	kg^{mes}	0.30	μM
Zoo. Mic.	Preference for Small Phy.	ρ_{11}	1.00	n.d.
Zoo. Mes.	Preference for Small Phy.	ρ_{12}	1.00	n.d.
Zoo. Mic.	Preference for Large Phy.	ρ_{21}	1.00	n.d.
Zoo. Mes.	Preference for Large Phy.	ρ_{22}	1.00	n.d.
Zoo.	Assim. efficiency	β_{zoo}	0.40	n.d.
Zoo.	Mortality specific rate	m_{zoo}	0.05	d^{-1}
Zoo.	Mortality fraction to POM	ω_{zoo}	0.50	n.d.
Zoo.	Non-assim. fraction to POM	ψ_{zoo}	0.50	n.d.
POM	Sinking rate	$\lvert\bar{w}\rvert$	0.50	m d^{-1}
POM	Degradation rate to DOM	m^{POM}	0.10	d^{-1}
DOM	Degradation rate to DOM	m^{DOM}	0.10	d^{-1}

AppendixC. Validation of the ecological model

Following Lefèvre et al. (2002), modelled chlorophyll was computed applying a variable C:Chl ratio calculated as a function of light levels following:

$$R_t = R_{max} - (R_{max} - R_{min}) \cdot (\frac{I_{max} - I_t}{I_{max} - I_{mix}}), \tag{C.1}$$

R represents the C:Chl ratio. R_{max} and R_min vary depending on phytoplankton size (R_{max}^{sma} = 200.00 mg C mg Chl^{-1}; R_{min}^{sma} = 166.67 mg C mg Chl^{-1}; R_{max}^{lar} = 111.11 mg C mg Chl^{-1}; R_{min}^{lar} = 90.91 mg C mg Chl^{-1}).

I is the photosynthetically active radiation (PAR; μEin m^{-2} s^{-1}) at the sea surface, derived from ERA-Interim and provided by the European Center for Medium-range Weather Forecast (ECMWF; https://www.ecmwf.int/; Dee et al., 2011). I_{max}, I_{min} and I_t, which represents the daily PAR, are obtained for each point of the model grid and at noon.

AppendixD. Eastward time-steps during neap and spring tides

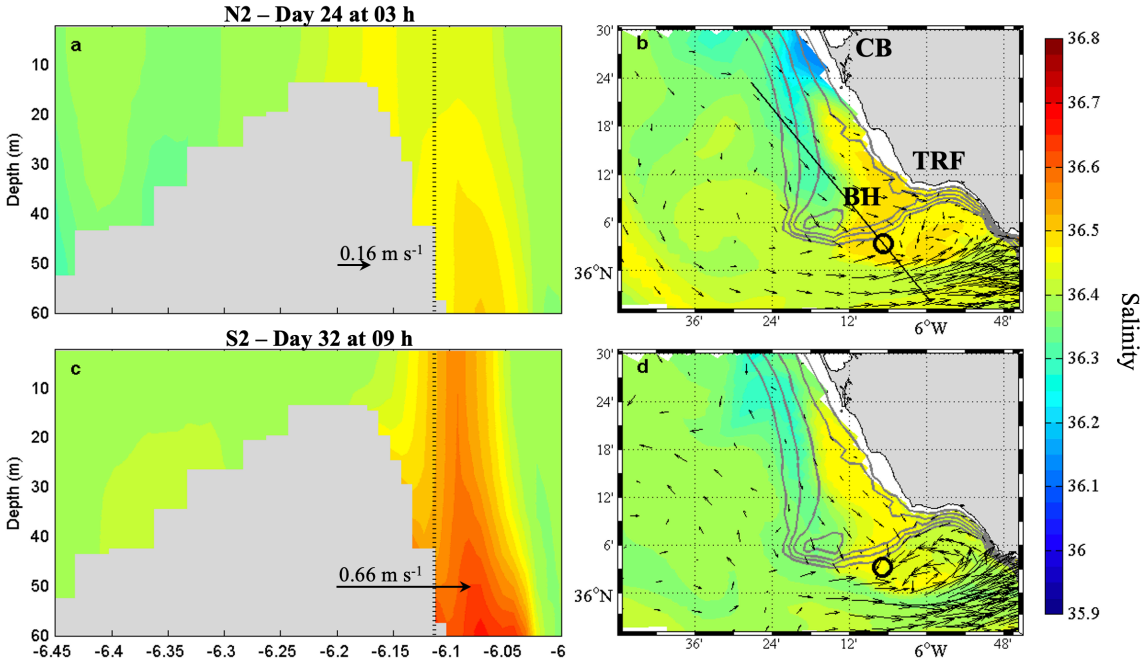

Figure D.1: Salinity distribution at the Cape Trafalgar region during the maximum eastward flow of the neap tide period (NT2: a, b) and the spring tide period (ST2: c, d) (see Figure 3). Left-hand panels show the vertical distribution along a section perpendicular to the submarine ridge (black line in panel b). Vertical dashed lines correspond to the position of open black circles in right-hand panels. Black arrows (a, c) represent the magnitude and direction of the mean zonal component of current velocity (uvel; m s^{-1}), computed for the whole water column at 6.11 °W and 36.06 °N at each time-step. Right-hand panels show the surface distribution. Black surface vectors represent the surface current (m s^{-1}). Grey solid lines represent the bathymetry (10, 20, 30, 40 and 50 m depth). BH: Barbate High. CB: Cádiz Bay. TRF: Cape Trafalgar.

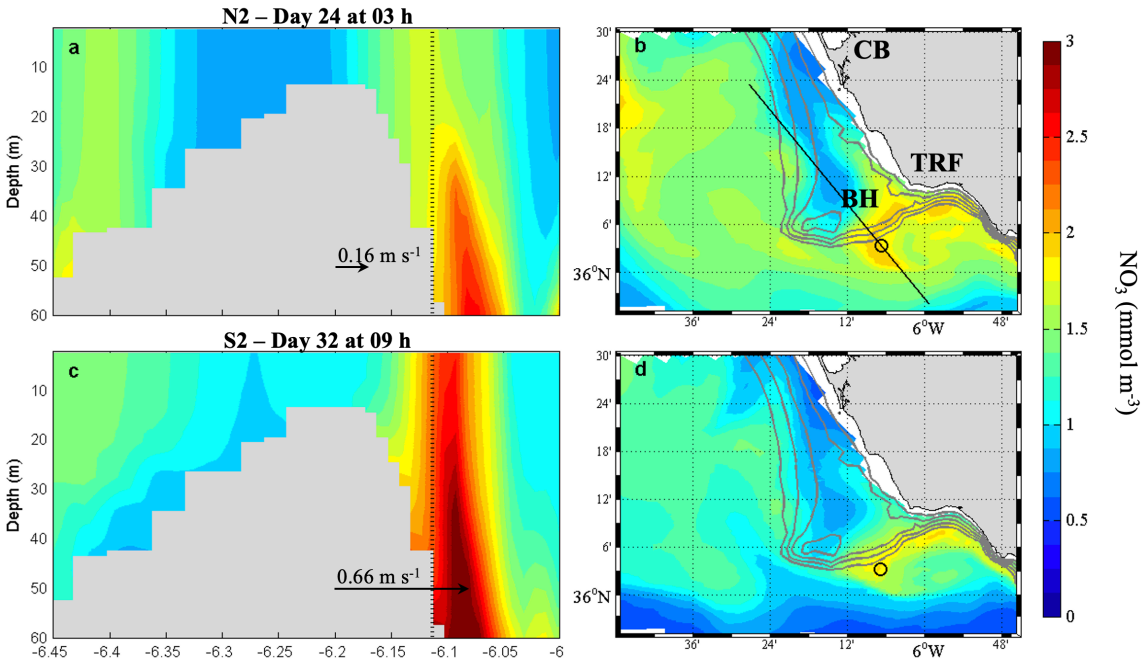

Figure D.2: Nitrate concentration (NO_3, mmol m^{-3}) distribution at the Cape Trafalgar region during the maximum eastward flow of the neap tide period (NT2: a, b) and the spring tide period (ST2: c, d) (see Figure 3). Left-hand panels show the vertical distribution along a section perpendicular to the submarine ridge (black line in panel b). Vertical dashed lines correspond to the position of open black circles in right-hand panels. Black arrows (a, c) represent the magnitude and direction of the mean zonal component of current velocity (uvel; m s^{-1}), computed for the whole water column at 6.11 °W and 36.06 °N at each time-step. Right-hand panels show the surface distribution. Grey solid lines represent the bathymetry (10, 20, 30, 40 and 50 m depth). BH: Barbate High. CB: Cádiz Bay. TRF: Cape Trafalgar.

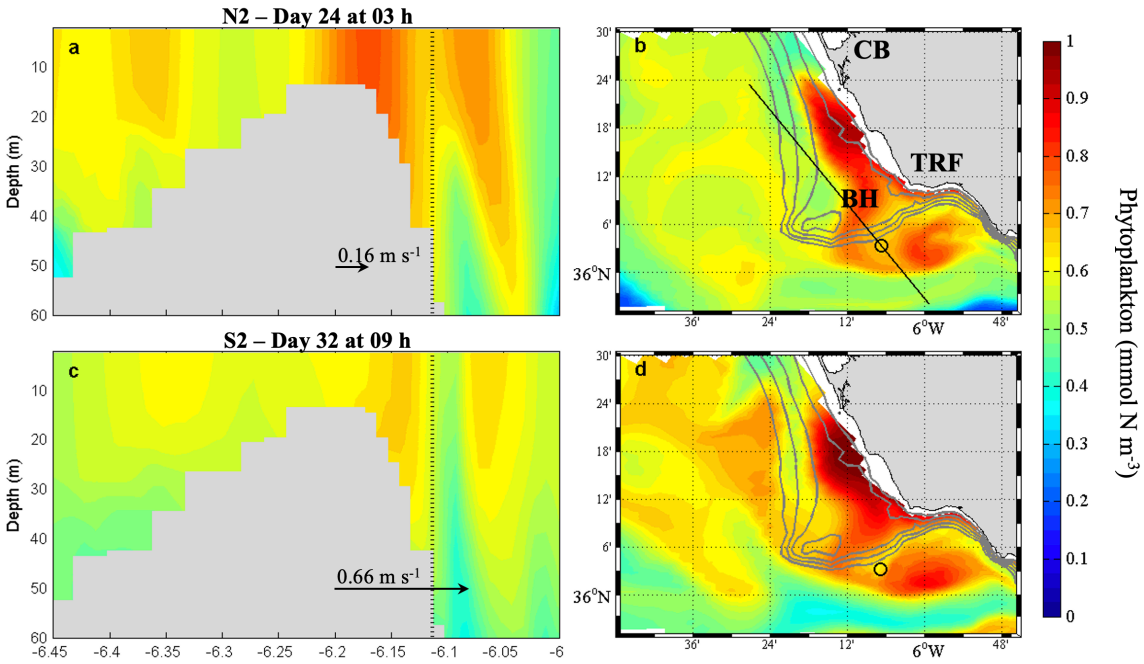

Figure D.3: Total phytoplankton biomass (mmol N m^{-3}) distribution at the Cape Trafalgar region during the maximum eastward flow of the neap tide period (NT2: a, b) and the spring tide period (ST2: c, d) (see Figure 3). Left-hand panels show the vertical distribution along a section perpendicular to the submarine ridge (black line in panel b). Vertical dashed lines correspond to the position of open black circles in right-hand panels. Black arrows (a, c) represent the magnitude and direction of the mean zonal component of current velocity (uvel; m s^{-1}), computed for the whole water column at 6.11 °W and 36.06 °N at each time-step. Right-hand panels show the surface distribution. Grey solid lines represent the bathymetry (10, 20, 30, 40 and 50 m depth). BH: Barbate High. CB: Cádiz Bay. TRF: Cape Trafalgar.

AppendixE. Analysis of the zonal component of the wind at 10 m

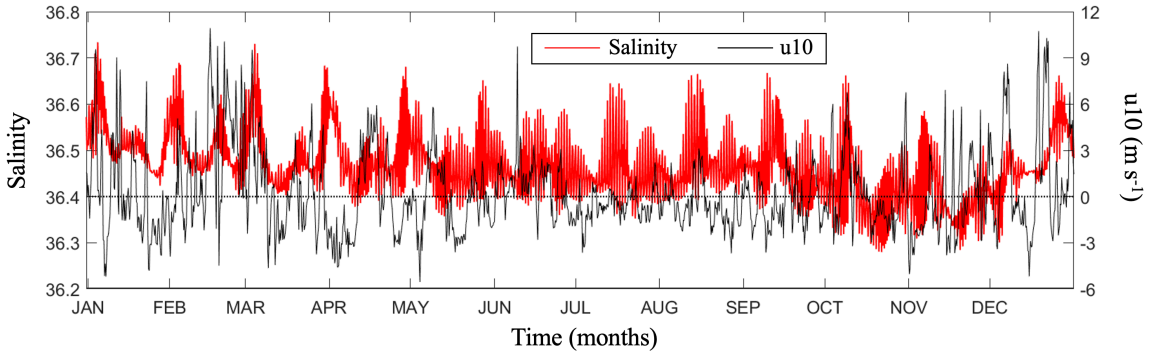

Figure E.1: Temporal evolution of salinity versus the zonal component of the wind at 10 m (u10, m s^{-1}) every 6 h at 6.11 °W and 36.06 °N (red circle in Figure 1b). The black horizontal line represents the zero u10 reference delimiting positive (negative) values that indicate westerly (easterly) winds.

References

Blauw, A.N., Benincà, E., Laane, R.W., Greenwood, N., Huisman, J., 2018. Predictability and environmental drivers of chlorophyll fluctuations vary across different time scales and regions of the North Sea. Progress in Oceanography 161, 1–18. doi:10.1016/j.pocean.2018.01.005.

Blauw, A.N., Benincä, E., Laane, R.W.P.M., Greenwood, N., Huisman, J., 2012. Dancing with the Tides: Fluctuations of Coastal Phytoplankton Orchestrated by Different Oscillatory Modes of the Tidal Cycle. PLoS ONE 7, e49319. doi:10.1371/journal.pone.0049319.

Bolado-Penagos, M., González, C.J., Chioua, J., Sala, I., Gomiz-Pascual, J.J., Vázquez, Á., Bruno, M., 2020. Submesoscale processes in the coastal margins of the Strait of Gibraltar. The Trafalgar – Alboran connection. Progress in Oceanography , 102219doi:10.1016/j.pocean.2019.102219.

Bruno, M., Chioua, J., Romero, J., Vázquez, Á., Macías, D., Dastis, C., Ramírez-Romero, E., Echevarría, F., Reyes, J., García, C.M., 2013. The importance of submesoscale processes for the exchange of properties through the Strait of Gibraltar. Progress in Oceanography 116, 66–79. doi:10.1016/j.pocean.2013.06.006.

Buttay, L., Cazelles, B., Miranda, A., Casas, G., Nogueira, E., González-Quirós, R., 2017. Environmental multi-scale effects on zooplankton inter-specific synchrony. Limnology and Oceanography 62, 1355–1365. doi:10.1002/lno.10501.

Cazelles, B., Chavez, M., Berteaux, D., Ménard, F., Vik, J.O., Jenouvrier, S., Stenseth, N.C., 2008. Wavelet analysis of ecological time series. Oecologia 156, 287–304. doi:10.1007/s00442-008-0993-2.

Cazelles, B., Stone, L., 2003. Detection of imperfect population synchrony in an uncertain world. Journal of Animal Ecology 72, 953–968. doi:10.1046/j.1365-2656.2003.00763.x.

Chen, C., Beardsley, R.C., 1998. Tidal mixing and cross-frontal particle exchange over a finite amplitude asymmetric bank: A model study with application to Georges Bank. Journal of Marine Research 56, 1163–1201. doi:10.1357/002224098765093607.

Costanza, R., Groot, R.d., Sutton, P., Ploeg, S.v.d., Anderson, S.J., Kubiszewski, I., Farber, S., Turner, R.K., 2014. Changes in the global value of ecosystem services. Global Environmental Change 26, 152–158. doi:10.1016/j.gloenvcha.2014.04.002.

Dale, A.C., Ullman, D.S., Barth, J.A., Hebert, D., 2003. The front on the northern flank of georges bank in spring: 1. tidal and subtidal variability. Journal of Geophysical Research: Oceans 108. doi:https://doi.org/10.1029/2002JC001327.

Daly, K.L., Smith, J.W.O., 1993. Physical-Biological Interactions Influencing Marine Plankton Production. Annual Review of Ecology and Systematics 24, 555–585. doi:10.1146/annurev.es.24.110193.003011.

Dee, D.P., Uppala, S.M., Simmons, A.J., Berrisford, P., Poli, P., Kobayashi, S., Andrae, U., Balmaseda, M.A., Balsamo, G., Bauer, P., Bechtold, P., Beljaars, A.C.M., Berg, L.v.d., Bidlot, J., Bormann, N., Delsol, C., Dragani, R., Fuentes, M., Geer, A.J., Haimberger, L., Healy, S.B., Hersbach, H., Hólm, E.V., Isaksen, L., Kållberg, P., Köhler, M., Matricardi, M., McNally, A.P., Monge-Sanz, B.M., Morcrette, J., Park, B., Peubey, C., Rosnay, P.d., Tavolato, C., Thépaut, J., Vitart, F., 2011. The ERA-Interim reanalysis: configuration and performance of the data assimilation system. Quarterly Journal of the Royal Meteorological Society 137, 553–597. doi:10.1002/qj.828.

Dutkiewicz, S., Follows, M.J., Bragg, J.G., 2009. Modeling the coupling of ocean ecology and biogeochemistry. Global Biogeochemical Cycles 23. doi:10.1029/2008gb003405.

Echevarría, F., García-Lafuente, J., Bruno, M., Gorsky, G., Goutx, M., González, N., García, C.M., Gómez, F., Vargas, J.M., Picheral, M., Striby, L., Varela, M., Alonso, J.J., Reul, A., Cózar, A., Prieto, L., Sarhan, T., Plaza, F., Jiménez-Gómez, F., 2002. Physical-biological coupling in the strait of gibraltar. Deep-Sea Research Part II: Topical Studies in Oceanography 49, 4115–4130. doi:10.1016/S0967-0645(02)00145-5.

Follows, M.J., Dutkiewicz, S., Grant, S., Chisholm, S.W., 2007. Emergent biogeography of microbial communities in a model ocean. Science 315, 1843–1846.

Franks, P., Chen, C., 2001. A 3-d prognostic numerical model study of the georges bank ecosystem. part ii: Biological–physical model. Deep Sea Research II 48, 457–482.

García, C.M., Prieto, L., Vargas, M., Echevarría, F., García-Lafuente, J., Ruiz, J., Rubín, J., 2002. Hydrodynamics and the spatial distribution of plankton and TEP in theGulf of Cádiz (SW Iberian Peninsula). Journal of Plankton Research 24, 817–833.

García-Lafuente, J., Almazán, J., Castillejo, F., Khribeche, A., Hakimi, A., 1990. Sea level in the Strait of Gibraltar: Tides. The International Hydrographic Review 67, 111–130.

Grinsted, A., Moore, J.C., Jevrejeva, S., 2004. Application of the cross wavelet transform and wavelet coherence to geophysical time series. Nonlinear Processes in Geophysics 11, 561–566. doi:10.5194/npg-11-561-2004.

Holloway, P.E., Chatwin, P.G., Craig, P., 2001. Internal tide observations from the australian north west shelf in summer 1995. Journal of Physical Oceanography 31, 1182 – 1199. doi:10.1175/1520-0485(2001)031<1182:ITOFTA>2.0.CO;2.

Hu, S., Townsend, D.W., Chen, C., Cowles, G., Beardsley, R.C., Ji, R., Houghton, R.W., 2008. Tidal pumping and nutrient fluxes on Georges Bank: A process-oriented modeling study. Journal of Marine Systems 74, 528–544. doi:10.1016/j.jmarsys.2008.04.007.

Huertas, E., Navarro, G., Rodríguez-Gálvez, S., Prieto, L., 2005. The influence of phytoplankton biomass on the spatial distribution of carbon dioxide in surface sea water of a coastal area of the Gulf of Cdiz (southwestern Spain). Canadian Journal of Botany 83, 929–940. doi:10.1139/b05-082.

Hundsdorfer, W., Trompert, R., 1994. Method of lines and direct discretization: a comparison for linear advection. Applied Numerical Mathematics 13, 469–490.

Ippen, A., 1966. Estuary and Coastline Hydrodynamics. McGraw-Hill Book Company Inc., New York, 744 pp.

Ji, R., Davis, C., Chen, C., Beardsley, R., 2008. Influence of local and external processes on the annual nitrogen cycle and primary productivity on Georges Bank: A 3-D biological–physical modeling study. Journal of Marine Systems 73. doi:10.1016/j.jmarsys.2007.08.002.

Keitt, T., Fischer, J., 2006. Detection of scale-specific community dynamics using wavelets. Ecology 87, 2895–2904.

Klvana, I., Berteaux, D., Cazelles, B., 2004. Porcupine Feeding Scars and Climatic Data Show Ecosystem Effects of the Solar Cycle. The American Naturalist 164, 283–297. doi:10.1086/423431.

Large, W.G., McWilliams, J.C., Doney, S.C., 1994. Oceanic vertical mixing: A review and a model with a nonlocal boundary layer parameterization. Reviews of Geophysics 32, 363–403. doi:10.1029/94rg01872.

Lau, K., Weng, H., 1995. Climate signal detection using wavelet transform: How to make a time series sing. Bulletin of the American Meteorological Society 76, 2391–2402.

Lefèvre, M., Vézina, M., Levasseur, M., Dacey, J.W., 2002. A model of dimethylsulfide dynamics for the subtropical north atlantic. Deep Sea Research I 49, 2221–2239.

Macias, D., García, C.M., Navas, F.E., Vázquez-López-Escobar, A., Mejías, M.B., 2006. Tidal induced variability of mixing processes on Camarinal Sill (Strait of Gibraltar): A pulsating event. Journal of Marine Systems 60, 177–192. doi:10.1016/j.jmarsys.2005.12.003.

Macías, D., Lubián, L., Echevarría, F., Huertas, I., García, C., 2008. Chlorophyll maxima and water mass interfaces: Tidally induced dynamics in the Strait of Gibraltar. Deep Sea Research Part I: Oceanographic Research Papers 55, 832–846. doi:10.1016/j.dsr.2008.03.008.

Macías, D., Martin, A.P., García-Lafuente, J., García, C.M., Yool, A., Bruno, M., Vázquez, A., Izquierdo, A., Sein, D., Echevarría, F., 2007a. Analysis of mixing and biogeochemical effects induced by tides on the atlantic-mediterranean flow in the strait of gibraltar through a physical-biological coupled model. Progress in Oceanography 74, 252–272. doi:10.1016/j.pocean.2007.04.006.

Macías, D., Navarro, G., Echevarría, F., García, C.M., Cueto, J., 2007b. Phytoplankton pigment distribution in the northwestern Alboran Sea and meteorological forcing: A remote sensing study. Journal of Marine Research 65, 523–543. doi:10.1357/002224007782689085.

Macías, D., Ramírez-Romero, E., García, C.M., 2010. Effect of nutrient input frequency on the structure and dynamics of the marine pelagic community: A modeling approach. Journal of Marine Research 68, 119–151. doi:10.1357/002224010793078979.

Mahowald, N., Luo, C., Corral, J.d., Zender, C.S., 2003. Interannual variability in atmospheric mineral aerosols from a 22-year model simulation and observational data. Journal of Geophysical Research: Atmospheres (1984–2012) 108. doi:10.1029/2002jd002821.

Marshall, J., Adcroft, A., Hill, C., Perelman, L., Heisey, C., 1997a. A finite-volume, incompressible Navier Stokes model for studies of the ocean on parallel computers. Journal of Geophysical Research: Oceans 102, 5753–5766. doi:10.1029/96jc02775.

Marshall, J., Hill, C., Perelman, L., Adcroft, A., 1997b. Hydrostatic, quasi-hydrostatic, and nonhydrostatic ocean modeling. Journal of Geophysical Research: Oceans 102, 5733–5752. doi:10.1029/96jc02776.

Ménard, F., Marsac, F., Bellier, E., Cazelles, B., 2007. Climatic oscillations and tuna catch rates in the indian ocean: a wavelet approach to time series analysis. Fisheries Oceanography 16, 95–104.

Millero, F.J., Poisson, A., 1981. International one-atmosphere equation of state of seawater. Deep Sea Research Part A. Oceanographic Research Papers 28, 625–629. doi:https://doi.org/10.1016/0198-0149(81)90122-9.

Navarro, G., Ruiz, J., 2006. Spatial and temporal variability of phytoplankton in the Gulf of Cádiz through remote sensing images. Deep Sea Research Part II: Topical Studies in Oceanography 53, 1241–1260. doi:10.1016/j.dsr2.2006.04.014.

Navarro, G., Ruiz, J., Huertas, I., García, C.M., Criado-Aldeanueva, F., Echevarría, F., 2006. Basin-scale structures governing the position of the deep fluorescence maximum in the Gulf of Cádiz. Deep Sea Research Part II: Topical Studies in Oceanography 53, 1261–1281. doi:10.1016/j.dsr2.2006.04.013.

New, A., Pingree, R.D., 1990. Evidence for internal tidal mixing near the shelf break in the bay of biscay. Deep Sea Research I 37, 1783–1803.

Oguz, T., Mourre, B., Tintoré, J., 2017. Modulation of frontogenetic plankton production along a meandering jet by zonal wind forcing: An application to the Alboran Sea. Journal of Geophysical Research: Oceans 122, 6594–6610. doi:10.1002/2017jc012866.

Otto, L., Zimmerman, J.T.F., Furnes, G.K., Mork, M., Saetre, R., Becker, G., 1990. Review of the physical oceanography of the north sea. Neth. J. Sea Res. 26, 161–238.

Palmer, M.R., Inall, M.E., Sharples, J., 2013. The physical oceanography of Jones Bank: A mixing hotspot in the Celtic Sea. Progress in Oceanography 117, 9–24. doi:10.1016/j.pocean.2013.06.009.

Pingree, R.D., Griffiths, D.K., 1978. Tidal fronts on the shelf seas around the British Isles. Journal of Geophysical Research: Oceans 83, 4615–4622. doi:10.1029/jc083ic09p04615.

Pingree, R.D., Mardell, G., Cartwright, D., 1981. Slope Turbulence, Internal Waves and Phytoplankton Growth at the Celtic Sea Shelf-Break [and Discussion]. Philosophical Transactions of the Royal Society A: Mathematical, Physical and Engineering Sciences 302, 663–682. doi:10.1098/rsta.1981.0191.

Prieto, L., García, C.M., Corzo, A., Ruiz, J., Echevarría, F., 1999. Phytoplankton, bacterioplankton and nitrate reductase activity distribution in relation to physical structure in the northern Alborán Sea and Gulf of Cadiz (southern Iberian Peninsula). Boletín del Instituto Español de Oceanografía 15, 401–411.

Ramírez-Romero, E., Macías, D., Bruno, M., Reyes, E., Navarro, G., García, C., 2012. Submesoscale, tidally-induced biogeochemical patterns in the Strait of Gibraltar. Estuarine, Coastal and Shelf Science 101, 24–32. doi:10.1016/j.ecss.2012.02.010.

Rippeth, T.P., Inall, M.E., 2002. Observations of the internal tide and associated mixing across the malin shelf. Journal of Geophysical Research: Oceans 107, 3–1–3–14. doi:https://doi.org/10.1029/2000JC000761.

Sala, I., Navarro, G., Bolado-Penagos, M., Echevarría, F., García, C.M., 2018. High-chlorophyll-area assessment based on remote sensing observations: The case study of Cape Trafalgar. Remote Sensing 10, 165. doi:10.3390/rs10020165.

Sánchez-Garrido, J.C., Naranjo, C., Macías, D., García-Lafuente, J., Oguz, T., 2015. Modeling the impact of tidal flows on the biological productivity of the Alboran Sea. Journal of Geophysical Research: Oceans 120, 7329–7345. doi:10.1002/2015jc010885.

Sarhan, T., García-Lafuente, J., Vargas, M., Vargas, J.M., Plaza, F., 2000. Upwelling mechanisms in the northwestern Alborán Sea. Journal of Marine Systems 23, 317–331.

Sharples, J., Tweddle, J.F., Green, J.A.M., Palmer, M.R., Kim, Y.N., Hickman, A.E., Holligan, P.M., Moore, C.M., Rippeth, T.P., Simpson, J.H., Krivtsov, V., 2007. Spring-neap modulation of internal tide mixing and vertical nitrate fluxes at a shelf edge in summer. Limnology and Oceanography 52, 1735–1747. doi:10.4319/lo.2007.52.5.1735.

Simpson, J.H., Sharples, J., 2012. Introduction to the Physical and Biological Oceanography of Shelf Seas. Cambridge University Press.

Sotillo, M.G., Cailleau, S., Lorente, P., Levier, B., Aznar, R., Reffray, G., Amo-Baladrón, A., Chanut, J., Benkiran, M., Alvarez-Fanjul, E., 2015. The MyOcean IBI Ocean Forecast and Reanalysis Systems: operational products and roadmap

to the future Copernicus Service. Journal of Operational Oceanography 8, 63–79. doi:10.1080/1755876x.2015.1014663.

Torrence, C., Compo, G.P., 1998. A practical guide to wavelet analysis. Bulletin of the American Meteorological Society 79, 61–78.

Vallina, S.M., Cermeño, P., Dutkiewicz, S., Loreau, M., Montoya, J., 2017. Phytoplankton functional diversity increases ecosystem productivity and stability. Ecological Modelling 361, 184–196. doi:10.1016/j.ecolmodel.2017.06.020.

Vallina, S.M., Follows, M.J., Dutkiewcz, S., Montoya, J., Cermeño, P., Loreau, M., 2014a. Global relationship between phytoplankton diversity and productivity in the ocean. Nature Communications 5, 4299. doi:10.1038/ncomms5299.

Vallina, S.M., Ward, B.A., Dutkiewicz, S., Follows, M.J., 2014b. Maximal feeding with active prey-switching: A kill-the-winner functional response and its effect on global diversity and biogeography. Progress in Oceanography 120, 93–109. doi:10.1016/j.pocean.2013.08.001.

Vargas-Yáñez, M., Sarhan, T., Plaza, J., Rubín, J.P., García-Martínez, M.C., 2002. The influence of tide-topography interaction on low-frequency heat and nutrient fluxes. Application to Cape Trafalgar. Continental Shelf Research 22, 115–139. doi:10.1016/S0278-4343(01)00063-2.

Vázquez, A., Flecha, S., Bruno, M., Macías, D., Navarro, G., 2009. Internal waves and short-scale distribution patterns of chlorophyll in the Strait of Gibraltar and Alborán Sea. Geophysical Research Letters 36. doi:10.1029/2009gl040959.